1	
2	
3	Earthquakes Drive Focused Denudation along
4	a Tectonically Active Mountain Front
5	
6	Gen Li ^{1*} , A. Joshua West ¹ , Alexander L. Densmore ² , Zhangdong Jin ³ , Fei Zhang ³ , Jin
7	Wang ³ , Marin Clark ⁴ , and Robert G. Hilton ²
8	
9	¹ Department of Earth Sciences, University of Southern California, Los Angeles, CA
10	90089, USA
11	² Institute of Hazard, Risk and Resilience and Department of Geography, Durham
12	University, Durham DH1 3LE, UK
13	³ State Key Laboratory of Loess and Quaternary Geology, Institute of Earth
14	Environment, Chinese Academy of Sciences, Xi'an 710075, China
15	⁴ Department of Earth and Environmental Sciences, University of Michigan, Ann
16	Arbor, MI 48109, USA
17	
18	
19	*corresponding author
20	Phone: +1-(213)740-5825
21	Email: genli@usc.edu
22	
23	
24	Manuscript accepted for publication in Earth and Planetary Science Letters
25	
26	

Abstract

27

Earthquakes cause widespread landslides that can increase erosional fluxes observed 28 over years to decades. However, the impact of earthquakes on denudation over the 29 longer timescales relevant to orogenic evolution remains elusive. Here we assess 30 erosion associated with earthquake-triggered landslides in the Longmen Shan range at 31 32 the eastern margin of the Tibetan Plateau. We use the M_w 7.9 2008 Wenchuan and M_w 6.6 2013 Lushan earthquakes to evaluate how seismicity contributes to the erosional 33 budget from short timescales (annual to decadal, as recorded by sediment fluxes) to 34 long timescales (kyr to Myr, from cosmogenic nuclides and low temperature 35 thermochronology). Over this wide range of timescales, the highest rates of 36 denudation in the Longmen Shan coincide spatially with the region of most intense 37 landsliding during the Wenchuan earthquake. Across sixteen gauged river catchments, 38 sediment flux-derived denudation rates following the Wenchuan earthquake are 39 closely correlated with seismic ground motion and the associated volume of 40 Wenchuan-triggered landslides ($r^2 > 0.6$), and to a lesser extent with the frequency of 41 high intensity runoff events ($r^2 = 0.36$). To assess whether earthquake-induced 42 landsliding can contribute importantly to denudation over longer timescales, we 43 model the total volume of landslides triggered by earthquakes of various magnitudes 44 over multiple earthquake cycles. We combine models that predict the volumes of 45 landslides triggered by earthquakes, calibrated against the Wenchuan and Lushan 46 events, with an earthquake magnitude-frequency distribution. The long-term, 47 landslide-sustained "seismic erosion rate" is similar in magnitude to regional 48 long-term denudation rates (~0.5-1 mm yr⁻¹). The similar magnitude and spatial 49 coincidence suggest that earthquake-triggered landslides are a primary mechanism of 50 long-term denudation in the frontal Longmen Shan. We propose that the location and 51 intensity of seismogenic faulting can contribute to focused denudation along a 52 high-relief plateau margin. 53

1. Introduction

54

- Mountain erosion affects rates and patterns of crustal deformation including
- seismogenic faulting [e.g., Steer et al., 2014] and flexural-isostatic responses [e.g.,
- 57 Molnar and England, 1990], and influences the geological carbon cycle and
- consequently the climate system [e.g., Raymo et al., 1988; Wang et al., 2016]. Large
- earthquakes are thought to play an important role in the denudation of
- 60 tectonically-active mountain ranges because they cause widespread landslides that
- generate large volumes of clastic sediment [Keefer, 1994; Larsen et al., 2010; Hovius
- et al., 2011; Parker et al., 2011; Wang et al., 2015a]. Delivery of landslide debris to
- rivers and the subsequent fluvial evacuation can increase erosion rates over years to
- decades [e.g., Hovius et al., 2011; Wang et al., 2015a]. However, over longer
- timescales relevant to orogenic evolution (10^4-10^6 yr) , the role of earthquakes in
- denudation remains less well constrained, even though the volume of seismically
- triggered landslides may be sufficient to partly or wholly counteract seismically
- induced rock uplift [Parker et al., 2011; Hovius et al., 2011; Li et al., 2014; Marc et al.,
- 69 2016a].

70

- Detailed mapping of landslides [e.g., Keefer, 1994; Parker et al., 2011; Li et al., 2014;
- Xu et al., 2015] and hydrological gauging of sediment fluxes [e.g., Hovius et al., 2011;
- Wang et al., 2015a] capture the aftermath of individual events. Across multiple events,
- landslide volume scales with earthquake magnitude [Keefer, 1994; Malamud et al.,
- 75 2004; Marc et al., 2016b]. Combined with return time statistics for earthquakes, this
- scaling relationship can yield an estimate of long-term landslide rate that should
- reflect a "seismic erosion rate" associated with repeated earthquakes, assuming fluvial
- evacuation of landslide debris [Keefer, 1994; Malamud et al., 2004; Lavé and
- 79 Burbank, 2004; Li et al., 2014; Marc et al., 2016a]. Keefer (1994) found that seismic
- 80 erosion rates are comparable to fluvial sediment yields measured in several regions.
- 81 Cosmogenic nuclide and thermochronology datasets allow us to expand this approach
- to consider denudation rates measured over longer timescales that encompass multiple
- earthquakes and that are more relevant to mountain belt evolution. In this study, we
- focus on the Longmen Shan region of central China, where the 2008 M_w 7.9
- Wenchuan and 2013 M_w 6.6 Lushan earthquakes allow us to make estimates of
- seismic erosion rates. We evaluate both the spatial distribution and magnitude of these
- rates in the context of datasets from fluvial sediment fluxes, cosmogenic nuclides, and
- low-temperature thermochronology [e.g., Kirby et al., 2002; Ouimet et al., 2009;
- 89 Godard et al., 2010; Liu-Zeng et al., 2011; Wang et al., 2015a].
- The steep Longmen Shan mountain range defines the eastern margin of the Tibetan
- Plateau. This region has been at the nexus of contentious debates over the importance
- of motion along shallow faults versus ductile flow of lower crust for collisional
- mountain building [e.g., Clark and Royden, 2000; Hubbard and Shaw, 2009]. Focused
- denudation along the steep topographic front of such plateau margins may exert an
- important influence on deformation [e.g., Beaumont et al., 2001]. However, the
- 97 relative roles of tectonic and climatic drivers of denudation and thus the link

between climate and the geodynamic processes – remain unresolved, both for the Longmen Shan [e.g., Ouimet et al., 2009; Godard et al., 2010; Liu-Zeng et al., 2011] and elsewhere. We aim to gain new general insight into the long-term role of seismic erosion in tectonically active mountains and how it may contribute to focused denudation along the eastern margin of the Tibetan plateau.

103 104

2. Setting

With elevations rising to higher than 5 km over a 50 km horizontal distance, the 105 eastern Longmen Shan flank represents one of Earth's steepest plateau margins [Clark 106 and Royden, 2000; Densmore et al., 2007; Burchfiel et al., 2008]. Several Yangtze 107 headwater rivers (mainly the Min Jiang, Fu Jiang, Tuo Jiang, Qingyi Jiang and Dadu 108 He) drain from the Longmen Shan into the Sichuan Basin (Figure 1a). A series of 109 dextral-thrusting, oblique-slip faults bound the mountain front and comprise the 110 Longmen Shan fault system [Densmore et al., 2007; Burchfiel et al., 2008]. The 111 bedrock geology consists mainly of Proterozoic basement granitoids and high-grade 112 metamorphic rocks, metamorphosed sedimentary rocks of a Paleozoic passive margin 113 sequence, unmetamorphosed sedimentary rocks associated with a Mesozoic 114 foreland-basin succession, and limited Cenozoic sediments [Burchfiel et al., 2008]. 115 Climatically, the Longmen Shan range is located at the transition between the 116 117 domains dominated by the east Asian monsoon and the westerlies. Across the Longmen Shan, average annual rainfall decreases from the margin (~1100 mm yr⁻¹) 118 towards the plateau (as low as $\sim 600 \text{ mm yr}^{-1}$) [Liu-Zeng et al., 2011]. This regional 119 climate pattern is largely determined by the high topography, which acts as an 120 121 orographic barrier and may also affect atmospheric circulation by heating of the atmosphere [Molnar et al., 2010 and references therein]. Precipitation is highly 122 seasonal, with most rainfall during the wet season from June to September.

123124

The M_w 7.9 Wenchuan earthquake on May 12th, 2008 initiated in the southern 125 Longmen Shan, near the town of Yingxiu, and ruptured northeastward for ~270 km 126 along the Longmen Shan fault system (Figure 1a) [Burchfiel et al., 2008; Shen et al., 127 2009]. The strong ground motion triggered > 56,000 landslides in the steep 128 mountainous topography (Figure 1a) [Parker et al., 2011; Li et al., 2014; Xu et al., 129 2014]. These seismically induced landslides introduced large volumes of clastic 130 sediment into the fluvial system, estimated to total ~3 km³ [Li et al., 2014]. Prior 131 work has aimed to understand the effects on sediment transport. Li et al. (2014) 132 133 documented the spatial pattern and volume of landsliding, and Li et al. (2016) 134 assessed the connectivity of these landslides to the river network as a means of understanding their behavior as sediment sources. Wang et al. (2015a) used data from 135 the Chinese Hydrology Bureau to quantify suspended sediment transport rates. After 136 the Wenchuan earthquake (2008-2012), suspended sediment fluxes from the Min 137 Jiang, Fu Jiang and Tuo Jiang catchments increased by 3 to 7 times compared to 138 pre-earthquake levels (2006-2007). Based on ¹⁰Be concentrations in quartz from Min 139 Jiang riverbed sands, West et al. (2014) suggested that bedload transport rates had 140 increased by a similar order of magnitude to those of suspended load. The present 141

study takes advantage of this prior work, including the landslide inventory and sediment fluxes, in order to compare spatial patterns of denudation across a range of timescales.

We use the M_w 6.6 Lushan event as an additional constraint on the magnitude of seismic erosion rates. The Lushan earthquake occurred on April 20th, 2013 in the southern Longmen Shan, 80 km south of the Wenchuan epicenter (Figure 1a). This event initiated on a ramp in the range-front blind thrust fault, in the footwall of the Wenchuan rupture [Wang et al., 2014]. As in the Wenchuan event, widespread landsliding occurred in the southern Longmen Shan range during the Lushan earthquake. Xu et al. (2015) reported more than 20,000 co-seismic landslides, with a total area of 18.88 km² and an estimated volume of 0.042 km³ across the region of the Lushan earthquake.

3. Materials and Approaches

3.1. Landslide inventory

For the Wenchuan earthquake, co-seismic and immediately post-seismic landslides (within six months after the earthquake) were mapped by Li et al. (2014). Landslide volumes were calculated from empirical landslide area-volume scaling relations [e.g., Larsen et al., 2010]. We assume that mapped landslides mainly resulted from the Wenchuan mainshock because we find that aftershocks contributed <5% of the total seismic moment release across the Longmen Shan, based on the seismic catalog spanning over six months following the mainshock [CSN Catalog, 2015]. This finding is consistent with observations from other earthquakes that suggest most landslides occur during the main shock [e.g., Roback et al., 2017]. Additional volume associated with post-seismic (e.g., storm-triggered) landslides is likely to be on the order of a few percent of the total landslide volume [Li et al., 2016 and references therein].

For the landsides triggered by the Lushan earthquake, we refer to the landslide inventory compiled by Xu et al. (2015), who also used empirical scaling relationships reported in Larsen et al. (2010) to estimate volumes from a landslide map based on satellite imagery. Xu et al. (2015) mapped Lushan landslides using images collected from April – May 2013, around five years after the Wenchuan earthquake but immediately after the Lushan event. Also, there is not much overlap between the mapping extents and the intensive shaking zones for the Lushan and Wenchuan events [Li et al., 2014; Xu et al., 2015]. Thus we expect limited influence on the mapped Lushan landslides from the Wenchuan earthquake.

3.2. Geomorphic characterization

In evaluating the spatial patterns of denudation in the Wenchuan region, we focus on three main catchments (Min Jiang, Fu Jiang and Tuo Jiang), comprising sixteen sub-catchments as delineated by Li et al. (2016) (Figure 1b and Table S1). SRTM30 digital elevation model (DEM) data have incomplete coverage of the study region, so we used void-filled SRTM90 DEM data for topographic analysis [Jarvis et al., 2008].

Slopes were calculated using standard algorithms provided in the ArcGIS platform (Figure 1d). Although the derived slopes vary as a function of DEM resolution [e.g., Larsen et al., 2014], the biases are systematic (e.g., Figure S1) so we expect little influence on the relative trends between different catchments. Relief was determined as the ranges of elevations in 2.5 km-radius and 5 km-radius circular windows. We also calculated the volumetric density of landslides (m³ km⁻², landslide volume per unit catchment area) within each studied catchment (Table S1) and along a swath profile A-A' (Figure 1f). We derived channel steepness indexes (k_{sn} , normalized to θ_{ref} = 0.45, cf. Ouimet et al., 2009; symbol notation listed in Table 1) using the Stream Profiler toolbox (http://www.geomorphtools.org). DEM cells with drainage area < 1 km² were excluded to remove colluvial landscapes [Li et al., 2016]. To characterize ground motion associated with the Wenchuan earthquake, we used gridded peak ground acceleration (PGA) data obtained from the USGS ShakeMap (USGS Hazard Program, http://earthquake.usgs.gov/earthquakes).

3.3. Hydrological data

Wang et al. (2015a) analyzed data from the Chinese Hydrology Bureau and calculated total suspended load fluxes and runoff from 16 gauging stations across the Longmen Shan catchments (Figure 1a). This data covered both the pre-Wenchuan (2006-2007) and the post-Wenchuan (2008-2012) time periods. Using this dataset, Li et al. (2016) derived the suspended load fluxes for sub-catchments, by taking the differences between fluxes gauged at one station and all neighboring upstream stations, following a mass balance principle [Li et al., 2016]. Three sub-catchments yielded negative sediment fluxes, attributed to large sedimentary sinks such as reservoirs. As in Li et al. (2016), these were excluded from analysis (catchments labeled as "N.A." in Figure 1b).

Based on the gauged discharge and catchment area, we derived annual runoff for sub-catchments using an analogous mass balance approach to that for calculating sediment fluxes. Wang et al. (2015a) suggested that high magnitude runoff events play an important role in post-Wenchuan suspended sediment transport. We explored different thresholds for high magnitude runoff and found that a 6 mm day⁻¹ threshold best correlated with denudation rates (Figure S2 in Supporting Information), close to the 5 mm day⁻¹ used by Wang et al. (2015a). We also calculated specific stream power (ω) adopting the approach of Burbank et al. (2003) (details in Supporting Information) using our compiled runoff and topography data.

3.4. Calculation of sediment flux-derived ("short term") denudation rates

The total mass flux from a river catchment (i.e., the denudation rate) includes suspended, bedload, and dissolved load. To calculate total denudation rates, we adopted the approach of Liu-Zeng et al. (2011), who determined a pre-Wenchuan earthquake ratio of dissolved load to suspended load of 19±6%, and a ratio of bedload to suspended load of 25±15%. After the earthquake (2009-2012), Jin et al. (2016) measured solute fluxes at two sites (Zhenjiangguan and Weizhou, Figure 1a) in the

- 230 Min Jiang catchment, yielding a post-earthquake dissolved:suspended load ratio of
- 19±7% (Table S3 and text in Supporting Information), similar to pre-earthquake
- estimates. Measurements of ¹⁰Be concentrations in detrital quartz from bed sediments
- collected in 2009-2010 [West et al., 2014] indicate that, after the earthquake, bedload
- increased by a similar factor as suspended load. Thus the bedload:suspended load
- ratio is likely to be similar to that reported prior to the earthquake, i.e., $25\pm15\%$.
- Using these ratios between the dissolved load, bedload and suspended load, we
- calculated total denudation fluxes (t yr⁻¹) from the suspended sediment fluxes and
- converted these to denudation rates (mm yr⁻¹), assuming material density of 2.65×10^3
- kg m⁻³ [cf. Liu-Zeng et al., 2011]. To account for low-relief, frontal plains, which are
- expected to contribute little to the denudation flux, we normalized the calculated
- denudation rates to the fraction of mountainous area (defined as areas > 800 m
- elevation) in each catchment (Figure 1b and Table S1). We have examined
- relationships between these denudation rates and various hydrological and
- 244 topographic metrics we have calculated for the Longmen Shan (Section 3.2, 3.3).

3.5. Compilation of long-term (kyr to Myr) denudation rates

- To characterize the denudation of the Longmen Shan over longer timescales, we
- compiled ¹⁰Be-derived catchment-scale millennial denudation rates [Ouimet et al.,
- 2009; Godard et al., 2010; Ansberque et al., 2015] and refer to a data set of bedrock
- cooling ages and corresponding exhumation rates across the mountain range from
- low-temperature thermochronology studies (apatite fission track (AFT), apatite
- 252 (U-Th)/He (AHe), zircon fission track (ZFT) and zircon (U-Th)/He (ZHe)), compiled
- by Tian et al. (2013) [data from Arne et al., 1997; Kirby et al., 2002; Richardson et al.,
- 254 2008; Godard et al., 2009; Wang et al., 2012; Tian et al., 2013]. Tian et al. (2013)
- converted the cooling ages to time-averaged exhumation rates assuming a
- one-dimensional, steady state upper crustal section and taking into account the effects
- of cooling rate on closure temperature together with heat advection during
- exhumation, following Reiners and Brandon (2006). For geothermal gradient, Tian et
- al. (2013) assumed a pre-exhumation geothermal gradient of 20 °C km⁻¹, which yields
- a syn-exhumation gradient of 23-30°C km⁻¹, consistent with the present geothermal
- 261 gradient in the Longmen Shan determined from thermal logging of local boreholes (>
- 4.5 km deep) and numerical modeling [Tian et al., 2013]. Uncertainties on the
- 263 exhumation rates were propagated from uncertainties on thermochronology
- measurements [Tian et al., 2013].

265266

267

3.6. Calculation of seismic erosion rate over multiple earthquake cycles

3.6.1. Approach to calculating seismic erosion rate

- Over multiple recurrence cycles, earthquakes of various magnitudes occur at different
- 269 frequency. To characterize the cumulative effect, we defined a seismic erosion rate
- 270 (mm yr⁻¹) as the total volume of landslides triggered over multiple earthquake cycles
- and over a specified area, following Keefer (1994):

	$\sum N(M_{_{W}}) \times V_{_{L}}(M_{_{W}})$	
273	$\dot{e} = \frac{M_{w}}{t \times A}$	(1)
274		

where t represents the total time (yr) over which repeated earthquakes are integrated, A is the area of the region of landslide occurrence, $N(M_w)$ is the number of landslide-triggering earthquakes in the magnitude bin $[M_w, M_w + 0.1]$, and $V_L(M_w)$ refers the corresponding landslide volume triggered by an earthquake of magnitude M_w .

Based on the Wenchuan landslide data, we assumed that all landslides have occurred within an intensive erosion zone along the frontal Longmen Shan (Section 4.1), with an area of 170 km×80 km (A). This area, to first order, matches the areal extent of landslide occurrence predicted for a M_w 8 event by Keefer (1994), and the length of this region also approximates the rupture length of the Wenchuan earthquake [Burchfiel et al., 2008]. By distributing the total volume of earthquake-triggered landslides over area A and time period t, we obtain a spatially and temporally averaged rate of seismic erosion.

To calculate a seismic erosion rate from Eq. 1, we adopted a numerical integration approach (after Keefer, 1994; see details in Supporting Information). This approach combines (1) a scaling relationship between earthquake magnitude and the volume of earthquake-triggered landslides (Section 3.6.2) and (2) a statistical description of earthquake magnitude and corresponding frequency throughout an earthquake sequence (Section 3.6.3). Summing the landslide volumes throughout a full earthquake sequence, we determined the total volume of landslides occurring over a time period *t* that captures multiple earthquake cycles, yielding a long-term seismic erosion rate (Eq. 1).

3.6.2. Earthquake magnitude-landslide volume scaling relations: predictive models of the total volume of earthquake-triggered landslides

Descriptions of the landslide volume associated with earthquakes range from simple empirical regression of volume versus earthquake magnitude [e.g., Keefer, 1994; Malamud et al., 2004] to models that seek to capture the mechanics of landslide triggering, including slope stability as it relates to hillslope angles and near-surface rock strength [e.g., Gallen et al., 2015; Marc et al., 2016b]. Large uncertainties plague the empirical regressions, whereas the more mechanistic models – although able to reproduce global patterns [e.g., Marc et al., 2016b] – include parameters that are often not precisely known, for example those describing rock strength, earthquake asperity depth, and ground motion attenuation. To capture this range of approaches, we estimated seismic erosion rates using both empirical regression and the model of Marc et al. (2016b). We also calculated rates with a Longmen Shan-specific landslide volume model based on locally-calibrated parameters and ground motion equations. To most accurately estimate seismic erosion rates for the Longmen Shan region, we

evaluated the predictions of these different models with reference to the observed landslide volumes from the Wenchuan and Lushan cases (see Section 5.1). The global empirical regression model, global seismologically-based model, and Longmen Shan-specific model are summarized as follows.

Global empirical regression: Keefer (1994) and Malamud et al. (2004) compiled a global dataset of landslide inventories triggered by large earthquakes. They reported a logarithmic scaling relation between the total volume of landslides triggered by an earthquake, V_L , and earthquake magnitude, M_w [Malamud et al., 2004]:

$$Log_{10}V_L = 1.42M_w - 11.26 (\pm 0.52)$$
 (2)

Global seismologically-based landslide model: Marc et al. (2016b) developed an approach to predict the total volume of earthquake-triggered landslides, taking into account seismogenic characteristics (e.g., seismic moment and asperity depth), landscape steepness, and material sensitivity (rock strength and pore pressure). We adopted this model using seismogenic and topographic parameters appropriate for the Wenchuan and Lushan earthquakes (see discussion in Section 4.3.1 and more details in Supporting Information).

 Longmen Shan-specific landslide model: Using local observations of ground motion attenuation, we derived an earthquake magnitude-landslide volume scaling relation specific for the Longmen Shan (details in Supporting Information). In brief, we first defined a landslide volume-PGA relation using the Wenchuan data (following Meunier et al., 2007; Figure S3a in Supporting Information). We combined this with a locally-calibrated equation describing ground motion attenuation in the Longmen Shan and neighboring areas [Cui et al., 2012; Wang et al., 2015b; and references therein]:

$$Log_{10}PGA = c_1 + c_2 M_w + c_3 Log_{10}(D + c_4)$$
(3)

where D represents distance to fault trace and c_1 , c_2 , c_3 and c_4 are empirical parameters, determined empirically from the Wenchuan data and other earthquakes in the Longmen Shan and neighboring region (see Figure S3b in Supporting Information). Combining the landslide volume-PGA relation and the PGA- M_w relation allows us to calculate the landslide volume for earthquakes across a range of earthquake magnitudes. The relation between earthquake magnitude and landslide volume can be well described by a logarithmic fit ($r^2 = 0.99$):

$$Log_{10}V_L = 23.77Log_{10}M_w - 11.91(\pm 0.07) \tag{4}$$

Slope angles also influence where landslides occur during earthquakes [Gallen et al., 2015; Marc et al., 2016b]. The Newmark model framework adopted by Gallen et al. (2015) accounts for slope angles but depends on assumptions about landslide

geometry, complicating its application in this case. However, consistent with studies of other earthquakes [Meunier et al., 2007], we find that in the case of the Longmen Shan PGA provides a good first-order empirical prediction of regional patterns in landslide occurrence without considering differences in slope angle (Figure S3a), perhaps because regional variability in slopes is relatively small when compared to PGA (Figure 1).

3.6.3. Longmen Shan earthquake sequence

Inferring a long-term seismic erosion rate from landslide volume predictions requires assumptions about the earthquake population over the timescales of multiple earthquake cycles. We simulated a sequence of earthquakes with various magnitudes using available seismological data from the Longmen Shan region. Because the Wenchuan earthquake ruptured almost the full length of the Longmen Shan frontal fault system [Burchfiel et al., 2008], M_w ~8 represents a reasonable upper bound for earthquake magnitudes in the study area. We chose $M_w \sim 5$ as a minimum magnitude for landslide triggering [Marc et al., 2016b]. The occurrence times of earthquakes of various magnitudes were determined using an earthquake frequency-magnitude distribution, with reference to regional historic seismicity data (China Earthquake Networks Center, 1657-2013) [Wang et al., 2015b] and results from paleoseismological and geodetic studies that suggest a recurrence interval (T) for Wenchuan-like events of 500 to 4000 years [Densmore et al., 2007; Shen et al., 2009; Thompson et al., 2015]. Across this range, the frequency-magnitude distribution of the Longmen Shan earthquakes could be well described using a truncated G-R function [Utsu, 1999 and references therein]. For the shortest estimated T (~500 years) [Thompson et al., 2015], Longmen Shan earthquake occurrence follows a classical, linear G-R relation.

 To estimate seismic erosion rates following Eq. 1, we integrated predictions of the landslide volumes across the simulated earthquake sequences. Predicted landslide volumes are sensitive to the source depth of each simulated earthquake (see details in Supporting Information). For the global seismologically-based model [Marc et al., 2016b], we assumed a scaling relation between earthquake magnitude and focal depth, calibrated using the Wenchuan and the Lushan data. For the Longmen Shan-specific model, we used the scaling between earthquake magnitude and focal depth to define a characteristic landslide-triggering depth for each earthquake magnitude. We assumed that only earthquakes shallower than this depth cause landslides. For a given magnitude, we estimated the proportion of events with a focal depth shallower than this threshold based on a local seismic catalog [CSN Catalog, 2015; see Figure S4].

3.6.4. Failure and resetting of hillslopes over earthquake cycles

In using scaling relationships to calculate seismic erosion rate over multiple earthquake cycles, we have assumed that for each event there are sufficient hillslopes that are prone to fail. Following one earthquake cycle, failed hillslopes need to be re-weakened and re-steepened to initiate new landsliding in the following earthquake

cycle. We estimate that for the Longmen Shan, the pace of hillslope resetting is 403 capable of keeping up with earthquake recurrence. For example, if we assume that the 404 landscape fails following a patchwork fashion, then each earthquake triggers 405 landslides on a different part of the unfailed landscape, allowing the failed hillslopes 406 time to recover [e.g., Parker et al., 2015]. During the Wenchuan earthquake, around 1% 407 408 of the high PGA-area (>0.2 g) was impacted by landsliding [Li et al., 2014]. Thus to fail the full landsliding-susceptible landscape would take ~100 earthquake cycles, or 409 50-400 kyrs (given an estimated return time of Wenchuan-like events of ~500-4000 410 vrs, see Section 3.6.3). If landscapes are steepened by river incision, the steepness 411 resetting time (i.e., time required for resetting the failed landscape to pre-Wenchuan 412 steepness) can be approximated as the ratio of the landslide depth versus the channel 413 incision rate. We estimate an average steepness resetting time of ~6-26 kyr, or ~2-50 414 earthquake cycles for the Longmen Shan region (based on a mean Wenchuan 415 landslide depth of ~6-13 m [Gallen et al., 2015] and a regional incision rate of ~0.5-1 416 mm yr⁻¹ [Tian et al., 2015 and references therein]). This resetting time is much shorter 417 than the 50-400 kyr to fully fail the landscape. Similarly, for a Longmen Shan 418 chemical denudation rate of ~0.1-0.2 mm yr⁻¹ [Liu-Zeng et al., 2011, and references 419 therein] we anticipate that re-weakening of hillslope material to a depth of ~6-13 m 420 would take 30-130 kyr. Therefore, regional channel incision and chemical weathering 421 422 propagation rates should be fast enough to re-steepen and re-weaken failed landscapes, rejuvenating hillslopes for landsliding over multiple earthquake cycles. 423

424 425

426

427

4. Results and Discussion

- 4.1. Intensive and persistent denudation along the frontal Longmen Shan across timescales, and its relation to seismically triggered landsliding
- 428 4.1.1. Zone of focused denudation
- Profiles of short-term denudation rates calculated from hydrological gauging and
- longer-term denudation rates from cosmogenic nuclides and thermochronology are
- shown in Figures 1 and 2, respectively. Rates are highest along the eastern Longmen
- Shan front and decrease towards the Tibetan Plateau along the A-A' trend. Based on
- these observations, we delineate an 80 km-wide zone of intensive erosion
- perpendicular to the strike of the mountain range (bounded by dashed blue lines in
- Figure 1c). This distinct zone features steep topography, maximum PGA, and the
- highest concentration of Wenchuan-triggered landslides (Figure 1c and Figure 1e).
- This region of intensive denudation was also identified by Liu-Zeng et al. (2011)
- based on denudation rates calculated from 1960s-1980s hydrological gauging data,
- though their rates were slightly higher (up to 0.5-0.8 mm yr⁻¹) than our pre-Wenchuan
- 440 (2006-2007) estimates (0.24 \pm 0.04 mm yr⁻¹). The difference is consistent with
- background declines in both water discharge and sediment flux in the Yangtze basin
- over the past 50 years, attributed in part to decreased precipitation as well as to human
- activities like dam building [Yang et al., 2015].

- Long-term denudation rates (Section 3.5) along the A-A' trend (Figure 2a, b, c, d and
- e) are also higher (> 0.5 mm yr⁻¹) along the front of the eastern Longmen Shan,

compared to the western (plateau) side. The similarity to sediment flux-derived rates suggests a persistent denudation pattern across both modern and longer-term timescales. Both patterns are, to first order, similar to the distribution of the Wenchuan co-seismic landslides (Figure 2b, c, d and e). We suggest that seismicity associated with the Longmen Shan fault system, which runs along the front of the range, provides a mechanism for generating repeated landslides in this zone, as seen during the Wenchuan earthquake. The spatial coincidence of these landslides with measured denudation rates is consistent with landslides sustaining denudation fluxes across a wide range of timescales.

Additional second-order features in the exhumation data from the Longmen Shan include two local high rates to the west (Figure 2e), beyond the region of most active landsliding associated with the Wenchuan earthquake. The extent to which these high rates are also explained by earthquake-triggered landsliding is unclear, but some evidence suggests that they might be. The high exhumation rates around 160 km distance along the A-A' transect (Figure 2e) are located along the Wenchuan-Maowen fault (WMF, Figure 2f), another major thrust fault within the Longmen Shan. Rapid exhumation in this region has been attributed to active thrusting of the WMF in the late Cenozoic [Tian et al., 2013 and references therein]. Accompanying seismic activity could have triggered earthquake-triggered landsliding, converting uplifted mass to clastic sediment, enhancing denudation fluxes, and leaving imprints in the exhumation rates seen today. The other zone of locally elevated rates, closer to the plateau (Figure 2e), is less well-defined: moderately high values are recorded by the cosmogenic nuclides and seen in part of the AFT data from Arne et al. (1997) but not in other data (e.g., ZFT). A potential local maximum in denudation rate coincides with a local peak of seismic moment release (Figure 2f, A-A' distance around 200 km) as calculated from short-term historic seismicity (1970-2015) [CSN Catalog, 2015]. Local clustering of seismicity might indicate the potential for landslide-triggering earthquakes in this region. Further low-temperature thermochronology would help to better constrain the exhumation pattern across the Longmen Shan and the linkage between exhumation and co-seismic landsliding.

4.1.2. Seismic control on focused denudation of the Longmen Shan

In addition to seismicity, several other features also vary along the profiles shown in Figures 1 and 2, potentially influencing spatial patterns of denudation [e.g., Burbank et al., 2003; Ouimet et al., 2009]. To distinguish these effects, we have examined the relationships between denudation rates inferred from post-earthquake gauging data (2008-2012) and a group of metrics of topography (slope, relief), hydrology (mean annual runoff, proportion of runoff from high intensity runoff events), fluvial erosion potential (stream power and normalized channel steepness index), seismic shaking (PGA, distance to fault rupture as a metric for seismic energy release), and the density of earthquake-triggered landslides (Figures 3 and 4). Using principle component analysis (PCA), these metrics cluster into two statistically distinct groups that reflect mechanistically distinct processes: (1) a "seismic component", comprising PGA,

landslide volumetric density and distance to fault rupture; and (2) a "non-seismic component," comprising slope angles, relief, steepness index, and the hydrological metrics (for detailed PCA results, see Figure S5, Table S4 and Table S5 and text in Supporting Information).

Across the non-seismic metrics, post-Wenchuan denudation rates correlate positively but moderately ($r^2 = 0.36$, P < 0.05, Figure 3a) with the proportion of catchment runoff from high intensity runoff events (> 6 mm day⁻¹), consistent with the findings of Wang et al. [2015a]. Pre-Wenchuan denudation rates also show a moderate, positive correlation with intense runoff events ($r^2 = 0.33$, P < 0.05, Figure 3a), but with a shallower slope than post-earthquake rates. The steeper slope of the post-earthquake data indicates that the denudation rate has become more sensitive to hydrological conditions under enhanced sediment supply following the earthquake. We find no correlation between denudation rates and mean annual catchment runoff. There are also no statistically significant correlations between the post-Wenchuan denudation rates and other non-seismic metrics including channel steepness index and stream power (Figure 3b, c, d, e and f), perhaps because landscape steepness exceeds the threshold where these relationships are easily observed [e.g., Ouimet et al., 2009].

For seismic metrics (Figure 4), we find statistically significant correlations between post-Wenchuan denudation rates and catchment-scale mean PGA ($r^2 = 0.61$, p < 0.002, Figure 4a), catchment-scale maximum PGA ($r^2 = 0.64$, p < 0.001, Figure 4b), distance to the fault rupture ($r^2 = 0.67$, p < 0.001, Figure 4c), and the volumetric density of earthquake-triggered landslides ($r^2 = 0.66$, p < 0.01, Figure 4d). Although USGS ShakeMap PGA data do not include local site effects and topographic amplification that may affect landslide occurrence, we expect these to have limited influence on the first-order spatial patterns that indicate a seismic control on denudation rates.

Since the principal component analysis separates these seismic parameters from the non-seismic metrics, we do not expect cross-correlation between these two groups (e.g., between PGA and catchment slope or runoff, Figure S6) to bias our interpretations. Seismic intensity and denudation rates co-vary both across the plateau margin (i.e., along A-A'), and also along strike of the range. While the former gradient coincides to some extent with changes in relief, slope, and runoff, the latter does not, emphasizing the seismic role in denudation.

The spatial coverage of the longer-term denudation rate data is not sufficient to conduct a similar analysis, but the correlations described here show that seismicity in the Longmen Shan is not inextricably coupled to other parameters that influence denudation rates. The correlation between sediment flux-derived denudation rates and seismic parameters suggests that the coincidence of high denudation rates and intensive landsliding along the frontal Longmen Shan reflects a seismic driver of denudation, rather than a coincidental relationship with an underlying control by topographic or other non-seismic parameters. We expect that the seismic control on

post-earthquake denudation rates as observed via sediment fluxes would recur for repeated earthquakes, providing a mechanism for seismicity to influence the longer-term pattern and rate of denudation.

We next consider the theoretical magnitude of denudation rate sustained by earthquake-triggered landsliding over multiple earthquake cycles (Section 4.2). We then compare these estimated rates of seismic erosion with the rates measured across timescales (Section 4.3).

4.2. Quantifying seismic erosion rates

4.2.1. Predictions of landslide volumes

Calculating a seismic erosion rate following Eq. 1 depends on predicting landslide volumes associated with earthquakes of varying magnitude. In Figure 5, we show results from the three predictive landslide volume models considered here: the global empirical regression of Malamud et al. (2004), the global seismologically-based model of Marc et al. (2016b), and the Longmen Shan-specific model. We compare these predictions to the volumes of landslides triggered by the Wenchuan and Lushan earthquakes, as determined from landslide mapping [Li et al., 2014; Xu et al., 2015]. The global empirical regression systematically underestimates the volumes of the Wenchuan and the Lushan landslides (Figure 5a). The Longmen Shan model accurately predicts both the Wenchuan and the Lushan landslide volumes (Figure 5b). The global seismologically-based model of Marc et al. (2016b) fits the observations if

adjustable parameters in the model are tuned (Figures 5c,d).

In more detail, the results of the global model of Marc et al. (2016b) are sensitive to the adopted parameters, including landscape steepness, mean asperity depth and hillslope material sensitivity. Whereas slope and asperity depth can be determined from DEM and seismological data, respectively, we lack independent constraints on the term describing material sensitivity, which is related to rock strength and pore pressure. Using a global average material sensitivity (as reported by Marc et al., 2016b) and local parameters describing seismology and topography, this model under-predicts the landslide volumes for both the Wenchuan and the Lushan earthquakes (Figure 5c). The model fits the Wenchuan and the Lushan observations for increases in the material sensitivity term of 6 times and 4.3 times, respectively. Model results for a 5× increase in material sensitivity (determined by the minimization of the sum of the squared residuals) closely approximate both volumes (Figure 5d).

Differences in curvature between the two seismologically-based V_L - M_w relations (Figure 5b vs. 5d) derive from assumptions about ground motion attenuation and the landslide volume-ground motion scaling relation. Marc et al. (2016b) assumed (i) a linear relationship between landslide volume and ground motion, in contrast to the non-linear relationship from Wenchuan-specific observations (Figure S3), and (ii) a significant "saturation" effect of ground motion at high earthquake magnitude,

thought to describe attenuation of high-frequency (e.g., 1 Hz) spectral accelerations 579 [e.g., Boore and Atkinson, 2008]. Thus the Marc et al. (2016b) model predicts that 580 ground motion and landslide volumes should increase only slightly with magnitude 581 for large $(M_w > \sim 6.5)$ earthquakes. Since the magnitude dependence is small, a ~ 5 km 582 shallower asperity depth is needed in this model to explain the much greater landslide 583 volume from the Wenchuan earthquake $(M_w=7.9; V_L=2.7-4.4 \text{ km}^3)$ vs. the Lushan 584 event $(M_w=6.6; V_L=0.042 \text{ km}^3 \text{ from Xu et al., 2015, although Marc et al., 2016b})$ 585 quoted a lower volume for this event), assuming similar material sensitivity. 586

587 588

589 590

591

592

593

594

595

596

597

598

599

600

601 602

603

604

605

606

607

608

609

610

4.2.2. Seismic erosion rates

The Longmen Shan earthquake frequency-magnitude distribution depends on the recurrence interval for Wenchuan-like events, T (Section 3.6.3, Figure 6a); across the range of plausible estimates for T (~500-4000 years), we find a lower seismic erosion rate with longer T (Figure 5b). For a given T, the corresponding seismic erosion rate also differs depending on the landslide volume model (Figure S7). Using the Longmen Shan seismologically-based landslide volume model (Figure 5b), we calculate an erosion rate of 0.44-0.96 mm yr⁻¹ (with a central estimate of 0.51-0.81 mm vr⁻¹), which reduces to 0.34-0.81 mm vr⁻¹ (with a central estimate of 0.40-0.69 mm yr⁻¹) taking into account focal depth (Figure 6b). The rates calculated using the global empirical regression [Keefer, 1994] and the global seismologically-based model [Marc et al., 2016b] are lower than the result using our Longmen Shan-specific model. This outcome is not surprising, since the two former models underestimate the observed landslide volumes for Wenchuan and Lushan, a discrepancy that we attribute to uncertainties in applying globally-calibrated parameters to a specific region (see Section 4.3.1, above). On the other hand, using the global seismologically-based model with the \sim 5× increase in material sensitivity that captures the observed Longman Shan volumes (Figure 5d) yields a seismic erosion rate of 0.37-1.68 mm yr⁻¹, with a central estimate of 0.73-0.99 mm yr⁻¹, close to that calculated from the Longmen Shan-specific model although slightly higher because of the strong non-linearity of the global model. These comparisons emphasize the sensitivity of landslide erosion calculations to model assumptions, and particularly the importance of using locally calibrated parameters since global average values may not accurately reflect a specific region (as suggested by Keefer, 1994).

611612613

614

615

616

617

618

619

620

621

622

4.3. Comparing magnitudes of denudation rates across different timescales 4.3.1. Average denudation rate of the frontal Longmen Shan

The catchment area-weighted means (±1 standard deviation) of pre-Wenchuan and post-Wenchuan denudation rates inferred from hydrological gauging are 0.24±0.04 mm yr⁻¹ and 1.09±0.13 mm yr⁻¹ respectively. The equivalent average kyr-timescale cosmogenic nuclide-derived denudation rate is 0.55±0.05 mm yr⁻¹. For denudation over Myr timescales, we interpolate the exhumation rates in the intensive erosion zone and run 1,000,000 Monte Carlo random simulations to account for the uncertainties from individual exhumation rate estimates. The resulting Myr denudation rate is 0.61+0.14/-0.08 mm yr⁻¹ (uncertainties indicate the 16th and 84th

percentiles of the Monte Carlo results). The inferred seismic erosion rates over multiple earthquake cycles range from 0.34 to 0.81 mm yr⁻¹ across the range of plausible T values (500-4000 years), using the Longmen Shan-specific seismologically-based V_I - M_W relation.

627 628

623

624

625

626

629

4.3.2. Pre- and Post-Wenchuan earthquake sediment fluxes versus long-term denudation rate

The 2006-2007 pre-Wenchuan denudation rate calculated from sediment fluxes is 630 lower than the long-term denudation rate. The rate reported from the 1960s to 1980s 631 gauging data is higher than that calculated from the 2006-2007 data, but still slightly 632 lower than the long-term rate. In contrast, the post-Wenchuan sediment flux-derived 633 denudation rate is the highest amongst all observed denudation rates (Figure 7). The 634 long-term average denudation rates (i.e., from cosmogenics and thermochronology) 635 thus fall between the immediate pre- and post-earthquake values derived from 636 sediment fluxes. In general terms, this pattern is consistent with a conceptual model 637 for erosional dynamics over one complete earthquake cycle in which the 638 pre-earthquake rates reflect below-average values and the post-earthquake rates 639 reflect an immediate post-seismic denudational pulse [Ouimet, 2010]. However, given 640 the large variability in pre-earthquake rates (comparing 2006-2007 data vs. 641 1960s-1980s), it is difficult to use these data to evaluate quantitatively the extent to 642 which the post-earthquake pulse contributes to the long-term budget; considering the 643 2006-2007 data alone, the post-earthquake pulse would need to play a major role to 644 make the long-term value, but considering the data from the 1960s-1980s, this role 645 646 would need to be relatively small over the long term.

647 648

649

650

651

652

653

654

655

656

657

658

659

660

661

662

663

664

4.3.3. Seismic erosion rate vs. long-term denudation rate

Our best estimate of the seismic erosion rate (0.34-0.81 mm yr⁻¹, using the Longmen Shan-specific landslide volume model) is comparable to the measured long-term denudation rates of the frontal Longmen Shan (kyr denudation rate: 0.55±0.05 mm yr⁻¹; Myr exhumation rate: 0.61+0.14/-0.08 mm yr⁻¹) (Figure 7). Using the global seismologically-based model for landslide volumes yields a slightly higher calculated denudation rate via earthquake-induced landslides (0.37-1.68 mm yr⁻¹, with central estimate of 0.73-0.99 mm yr⁻¹; Figure S7). Denudation rates determined either from gauging data and long-term chronometers include mass loss via dissolved load in addition to via physical erosion. If dissolved load is mainly derived from weathering of landslide material [e.g., Emberson et al., 2016], the calculated seismic erosion rate should be directly comparable to the denudation rate. Significant non-landslide solute sources, such as from ground water release [e.g., Jin et al., 2016], would increase the denudation rate compared to the calculated seismic erosion rates, although such effects should be small since dissolved load represents a relatively low proportion of the total denudation flux (~20%, Section 3.4). Either way, additional dissolved load contributions would not explain a lower measured denudation rate compared to the calculated seismic erosion rate.

We recognize that not all landslide material is necessarily evacuated from a mountain 667 belt by rivers within one earthquake cycle. Landslide erosion rates could be higher 668 than actual measured long-term denudation rates if new seismically triggered 669 landslides re-mobilize debris associated with prior earthquakes. Given the relatively 670 rapid rates of sediment evacuation observed in the Longmen Shan region compared to 671 672 the long earthquake recurrence times [Liu et al., 2013] and the lack of extensive storage of intra-montane landslide debris in this setting [Parker et al., 2011], we view 673 near-complete evacuation as a reasonable first-order assumption for comparing rates. 674 If this is the case, the seismic erosion rates calculated from the Longmen 675 Shan-specific landslide volume model are consistent with the measured long-term 676 denudation rates. 677

678 679

680

681

682

683

684

685

Whether the seismic erosion rate is similar in magnitude or slightly higher than the measured long-term rate (Figure 7), our results demonstrate that, at least in this region, earthquake-triggered landslides are capable of sustaining denudation rates that are comparable to long-term averages at the mountain belt scale and over timescales of multiple seismic cycles. A corollary is that the observed erosional fluxes are likely to be dominated by material derived from earthquake-triggered landslides, with implications not only for sediment dynamics and landscape evolution, but also for biogeochemical cycles [e.g., Jin et al., 2016; Emberson et al., 2016].

686 687 688

689

690

691

692

693

694

695

696

697

698

699

700

701

702

Over longer timescales, climate fluctuations may influence the capacity of the sediment routing systems for removing landslide debris and maintaining river incision and hillslope weathering rates required to sustain landslides. Indeed, we find that high intensity runoff events help to explain the observed short-term denudation rates in the Longmen Shan (Fig. 3a), pointing to the importance of climate variability as an erosional agent. Thus we expect that climate – which may have changed in response to topographic evolution [e.g., Molnar et al., 2010] – interacts with seismic events to influence the pace of surface processes in the Longmen Shan, even though a primary control may be related to the seismotectonic processes that trigger landslides and thus convert rocks to erodible sediment. Our results suggest that earthquake-triggered landslides can focus denudation in mountains where rivers have the capacity to transport and export the excess sediment supplied from hillslopes (e.g. Fig. 3a). In these settings the denudation can be considered as tectonically limited [Montgomery and Brandon, 2002], yet fully understanding topographic evolution will require better understanding how landslide frequency and magnitude, and the associated fluvial export of sediment, respond to long-term climatic fluctuations.

703704705

706

707

708

709

710

5. Conclusions and Implications

By considering the effects of multiple earthquakes, we calculate that co-seismic landslides can sustain denudation rates that are similar to the rates recorded by chronometers over timescales of thousands to millions of years (Figure 7). In addition to similar magnitudes, we find a first-order spatial coincidence of long-term denudation and Wenchuan-triggered landslides (Section 4.1, Figure 2), and a

correlation between the sediment-derived denudation rates and co-seismic landsliding (Figure 4d). Over the long term, the location of earthquake-triggered landslides should reflect earthquake sources and ground motion attenuation, with landslide density decreasing away from seismogenic faults [Meunier et al., 2007], as we also observe for the Wenchuan case.

715 716 717

718

719

720

721 722

723

724

725

726

727

728

729 730

731

711

712

713

714

Our observations suggest that the long-term location and rate of denudation in the Longmen Shan is consistent with the focusing of seismic energy release along range-bounding faults, with the resulting landslides serving as a primary mechanism sustaining denudation fluxes. Landslides can only continue to operate as effective denudation mechanisms if hillslopes are sufficiently steep. It is likely that the combination of uplift, river incision, and fluvial evacuation of sediment [e.g., Burbank et al., 1996; Bennett et al., 2016] is capable of continually re-steepening and re-weakening failed landscapes between earthquake cycles. Earthquakes should increase the efficiency of landslide generation for a given steepness and hillslope strength, such that the location of most intense erosion at the orogenic scale may be determined by seismic energy release. These effects could be enhanced by rock weakening resulting from greater deformation and orographic rainfall close to mountain fronts [Gallen et al., 2015; Vanmaercke et al., 2017]. We thus suggest that focused denudation along a high-relief plateau margin may be regulated at least in part by the location and activity of seismogenic faulting, and specifically by the resulting earthquake-triggered landslides.

732733734

Acknowledgements

- 735 This research was supported by the U.S. National Science Foundation
- 736 (NSF-EAR/GLD grant 1053504 to A.J.W.) and the Chinese Academy of Sciences
- 737 (YIS fellowship grant 2011Y2ZA04 to A.J.W.). G.L. was supported by the USC
- 738 Dornsife College Merit Fellowship and a GSA graduate student research grant. This
- work benefited from conversations with Sean Gallen, Niels Hovius, Odin Marc,
- Haoran Meng, Joel Scheingross, James Dolan and Seulgi Moon. We thank
- constructive comments from an anonymous reviewer that greatly helped to improve an earlier version of the manuscript and An Yin for editorial handling.

743

Figure 1.

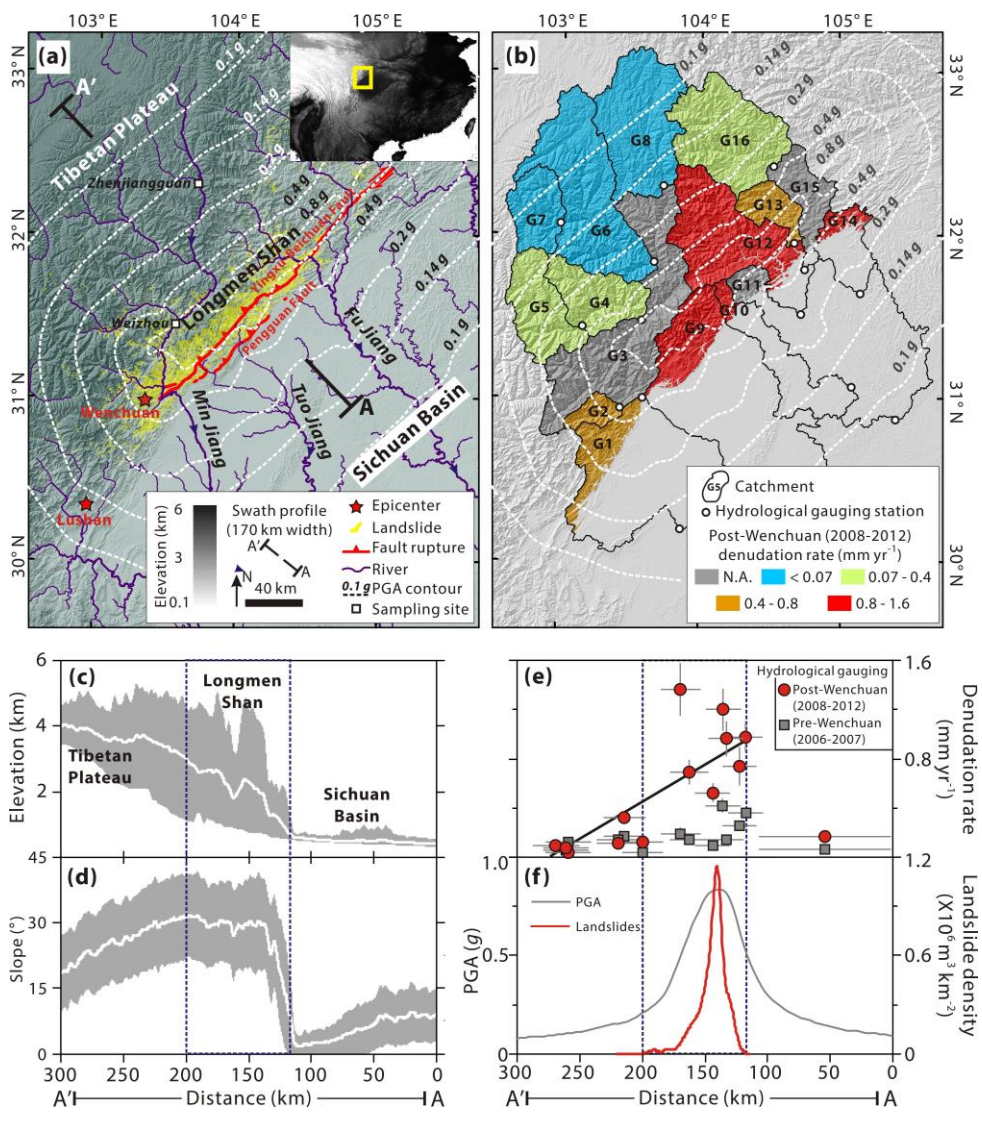
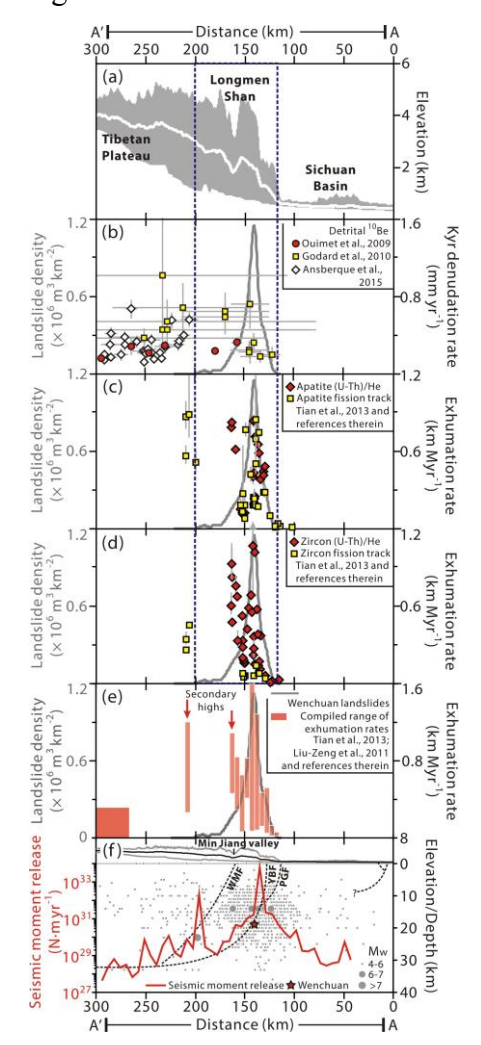


Figure 1. Maps of topography of the study area, locations of the M_w 7.9 2008 Wenchuan and the M_w 6.6 2013 Lushan earthquakes, the Wenchuan peak ground accelerations (PGA) (gridded data from the USGS hazards program, http://earthquake.usgs.gov/earthquakes), Wenchuan-triggered landslides and post-Wenchuan gauging-derived denudation rates, and swath profiles of topography, denudation rates, PGA, and landslides. (a) Map of the M_w 7.9 2008 Wenchuan earthquake and the M_w 6.6 Lushan earthquake epicenters (red stars), mapped Wenchuan earthquake-triggered landslides (yellow polygons) over shaded relief map, Wenchuan PGA contours (dashed lines), the trend of the 170 km-wide swath profile (A-A'), sampling sites of river water samples (Jin et al., 2016) (squares), Wenchuan earthquake surface rupture (red lines), and the regional context of the study area (inset panel); (b) map of post-seismic sediment flux-derived denudation rates upstream of hydrological gauging stations (circles); denudation rates are normalized to areas with

elevation > 800 m to account for limited contribution from flat frontal plains; (c) 764 swath profile of the topography projected along A-A' showing the mean (white line) 765 and maximum and minimum elevations (grey area); blue dashed lines delimit the zone 766 with intensive denudation between profile distances of 120 km and 200 km); (d) 767 swath profile of slopes (°) projected along A-A' with mean slope (white line) ± 1 768 769 standard deviation on the mean slope (grey area); (e) swath profile of pre-Wenchuan earthquake (2006-2007, red circles) and post-Wenchuan earthquake (2008-2012, grey 770 squares) denudation rates (y-axis error bars = ± 1 s.d. uncertainties in denudation rates, 771 x-axis error bars = square root of catchment area), the decreasing trend of 772 post-seismic denudation rates along the swath is shown by least-squares fitting of 773 denudation vs. distance along A-A' (solid black line); for denudation in the frontal 774 775 Sichuan basin, we divide the estimated denudation fluxes by the total catchment area including areas with elevation < 800 m, and this provides an upper limit; (f) swath 776 profiles sampled at 5 km-intervals along A-A' of PGA (grey) and the volumetric 777 density for all landslides (red, m³ km⁻², landslide volume over the specified area). 778

780 Figure 2.

779



781 782

783

784

785

786

787

788

789 790

791

792

793

794

795

796

797

Figure 2. Swath profiles of topography, millennial denudation rates, geological exhumation rates and seismicity across the Longmen Shan range. (a) Swath profile of topography along the Longmen Shan range (A-A'); white line – mean elevations; grey area – minimum-maximum elevation envelop; blue dashed lines bound the intensive denudation zone as defined in Figure 1; (b) swath profile of ¹⁰Be-derived millennial denudation rates; error bars on the y-axis indicate ± 1 s.d. uncertainties, and on the x-axis the square roots of the catchment area; (c) swath profile of apatite fission track (AFT) and apatite (U-Th)/He (AHe)-determined exhumation rates; error bars are ± 1 s.d. uncertainties; (d) swath profile of zircon (U-Th)/He (ZHe) and zircon fission track (ZFT)-determined exhumation rates with ± 1 s.d. uncertainties (error bars); (e) swath profile of compiled exhumation rates (red bars: range of exhumation rates including uncertainties; for data with distance < 250 km, data points are binned in 5 km-wide increments); the grey curves on (b), (c), (d) and (e) show the Wenchuan landslide distribution, as in Figure 1f; (f) swath profiles of topography (black solid curve: mean elevations; grey solid curves: minimum and maximum elevations), historic seismicity (1970-2015, grey circles sized by the estimated magnitude; star: Wenchuan

earthquake) [CSN Catalog, 2015] and seismic moment release (red curve, data binned in 5 km-wide increments), and a simplified sketch of the Longmen Shan fault system (WMF: Wenchuan-Maowen fault; YBF: Yingxiu-Beichuan fault; PGF: Pengxian-Guanxian fault) [Liu-Zeng et al., 2011; Ansberque et al., 2015 and references therein].

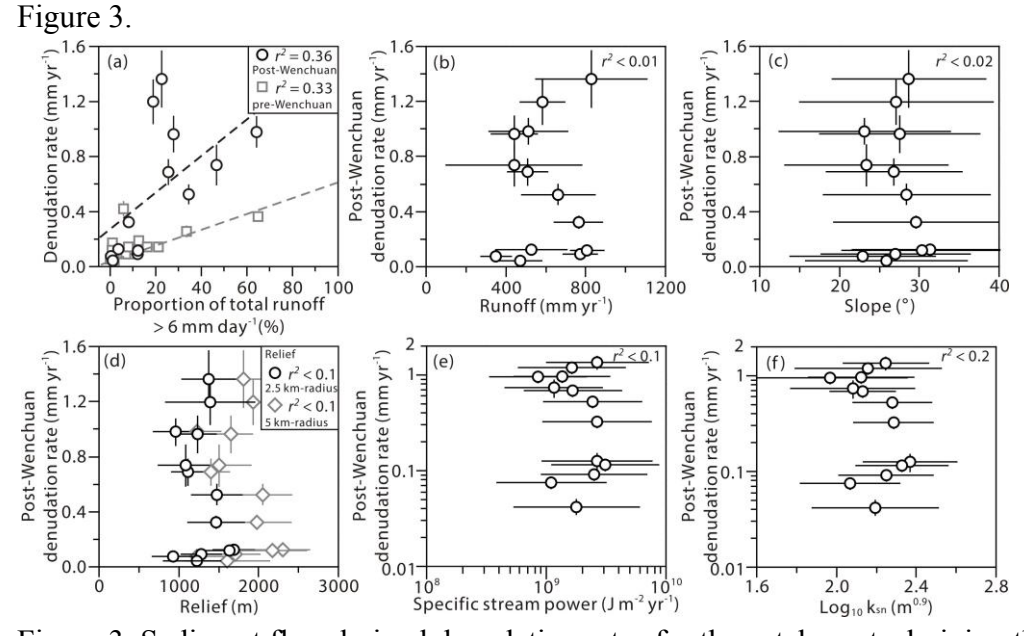


Figure 3. Sediment flux-derived denudation rates for the catchments draining the Longmen Shan plotted versus hydrological and topographic metrics. (a), Post-Wenchuan (circles) and pre-Wenchuan (squares) denudation rate as a function of the proportion of total runoff from days with runoff > 6 mm day⁻¹; post-Wenchuan denudation rate plotted versus annual runoff (b), slope (c), and relief (d); relief is calculated as the ranges of elevations over 2.5 km-radius (circles) and 5 km-radius (diamonds) circular windows. (e), Post-Wenchuan denudation rate against specific stream power calculated using the approach in Burbank et al., (2003) and Ansberque et al. (2015). (f), Post-Wenchuan denudation rate vs. normalized channel steepness index calculated using Stream Profiler (http://www.geomorphtools.org) and normalized to $\theta_{ref} = 0.45$. All error bars represent ± 1 s.d. uncertainties.



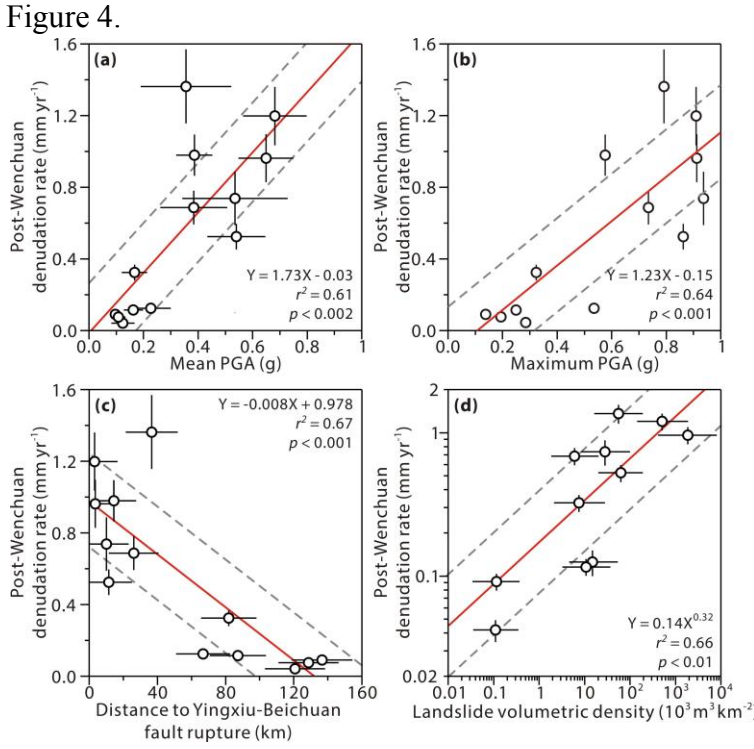
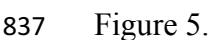


Figure 4. Relationships between sediment flux-derived denudation rates and seismic parameters. Post-Wenchuan denudation rate as a function of: (a) catchment mean PGA; (b) catchment maximum PGA; (c) mean distance of each catchment to the Yingxiu-Beichuan fault rupture; and (d) landslide volumetric density. Red solid lines show best fits from linear least-squares regression (performed in the logarithmic space for d); grey dashed lines show ± 1 s.d. uncertainties of the fits; error bars for denudation and PGA indicate ± 1 s.d. uncertainties; error bars for distance to the fault rupture are the square roots of catchment area; landslide volumetric densities are reported as the median values and the 16^{th} and 84^{th} percentiles of the distribution (i.e., ranges of ± 1 s.d. in a standard normal distribution) from the results from 1000 Monte Carlo random sampling simulations.



838

839

840

841

842

843

844

845

846

847

848

849

850

851

852

853

854

855

856

857

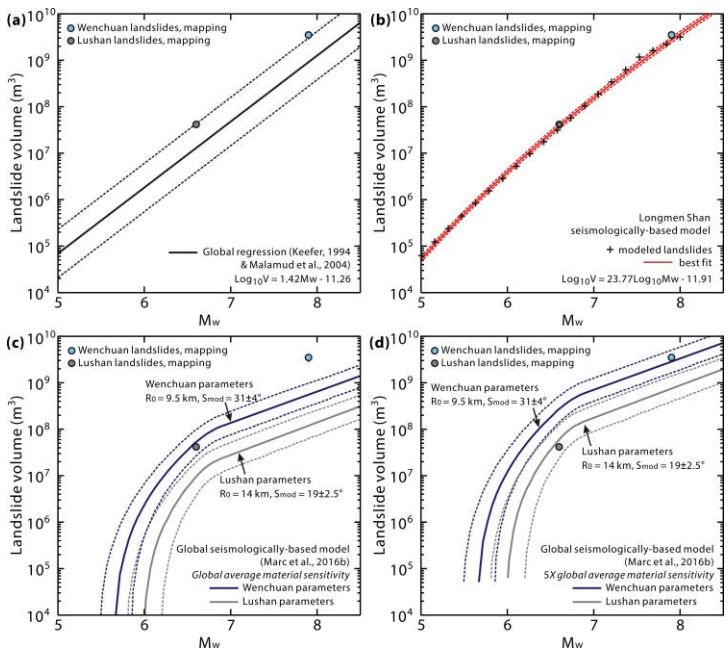


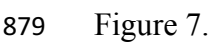
Figure 5. Earthquake-triggered landslide volume models. (a) Global empirical regression between earthquake magnitude and associated landslide volume [Keefer. 1994; Malamud et al., 2004]; solid line represents the logarithmic least squares linear fit; dashed lines show ± 1 s.d. uncertainties (residual errors) of the fit; the blue and the grey circles are Wenchuan and the Lushan data, respectively; (b) Longmen Shan-specific, seismologically-based landslide volume model; the crosses represent the modeled landslide volumes for 20 earthquakes with magnitude from 5 to 8; the solid curve represents the best fit of the modeled landslide volumes as a function of earthquake magnitude (details in the Supporting Information); the dashed curves show ±1 s.d. uncertainties (residual errors) of the fit; (c) a global seismologically-based landslide volume model [Marc et al., 2016b]; the blue and grey curves refer to the modeled landslide volumes using the Wenchuan parameters (mean asperity depth = 9.5 km, modal slope = $31\pm4^{\circ}$, uncertainty: range at 98% of modal slope frequency defined in Marc et al., 2016b) and the Lushan parameters (mean asperity depth = 14 km, modal slope = 19±2.5°, uncertainty: range at 98% of modal slope frequency defined in Marc et al., 2016b), respectively, both using global average material sensitivity; dashed curves show 68% confidence interval from Monte Carlo simulations accounting for uncertainties of the relevant parameters (Marc et al., 2016b; details in Supporting Information); (d) the modeled results from the model of Marc et al. 2016b with 5× material sensitivity.



Figure 6. (a) 1 10-1 (b) 2 10-1 10-1 G-R T = 500-4000 yr Menchuan Longmen Shan seismologically-based model

Figure 6. Earthquake magnitude-frequency distribution of the Longmen Shan region, and the calculated seismic erosion rate. (a) Longmen Shan earthquake magnitude-frequency relation described by a truncated Gutenberg-Richter relation [Utsu, 1999] using historic seismicity data (white circles) [Wang et al., 2015b] and the recurrence interval (T) for Wenchuan-like events from paleoseismological/geodetic studies (grey-shaded zone); red dot and solid curve – truncated G-R relation for T = 3000 years [Shen et al., 2009]; dashed line – linear G-R relation, which fits T ~ 500 years [Thompson et al., 2015]; (b) calculated seismic erosion rate with the Longmen Shan seismologically-based landslide volume model as a function of the estimated recurrence interval for Wenchuan-alike events, T; shaded area shows ±1 s.d; the solid curve shows results assuming landslides are triggered by all simulated earthquakes; the dashed curve includes a threshold focal depth for earthquake triggering.

---- Farthquake focal depth corrected



880

881

882

883

884

885

886

887

888

889

890

891

892

893

894

895

896 897

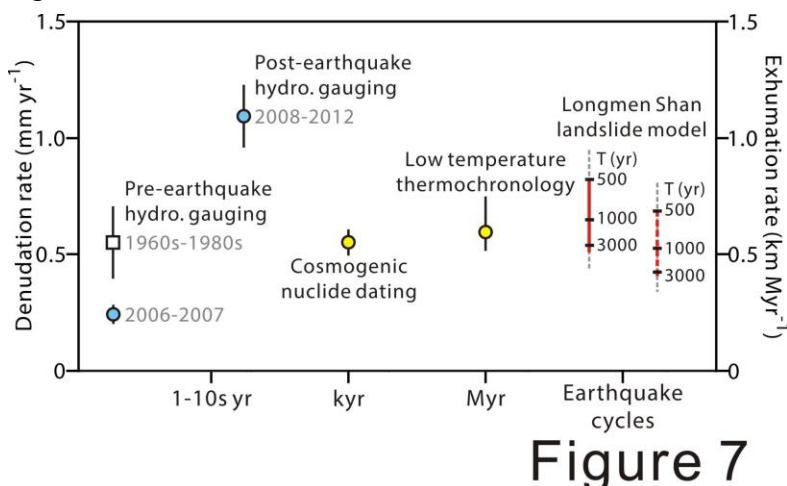


Figure 7. Denudation rates of the frontal Longmen Shan across different timescales. The blue circles show pre-Wenchuan and post-Wenchuan earthquake denudation rates determined from hydrological gauging; the square shows pre-Wenchuan earthquake (1960s-1980s) denudation rates reported in Liu-Zeng et al. (2011); vellow circles show long-term denudation rates determined from ¹⁰Be measurements and low temperature thermochronology analysis (AFT and AHe). For catchment-scale denudation (river gauging and ¹⁰Be studies), the denudation rates are the catchment area-weighted means, and the error bars represent catchment area-weighted 1 s.d. uncertainty. For the low temperature thermochronology-based denudation estimate, the denudation rate is reported as the average after interpolating the exhumation data compiled in Tian et al. (2013), with uncertainties propagated from the reported uncertainties in individual exhumation rate estimate [Tian et al., 2013]. Red bars with black ticks show seismic erosion rates across the range of estimated Wenchuan recurrence intervals (T=500-4000 years), with a solid red bar for all earthquakes, a dashed red bar considering focal depth threshold (see Fig. 6), and black ticks for noted T values; dashed grey line = 1 s.d. uncertainties.

Table 1. Notation for symbols

Symbol	Notation	Unit
A	Area of landslide occurrence over earthquake cycles	km ²
$c_1 c_2 c_3 c_4$	Parameters of ground motion attenuation equation, Longmen Shan	
D	Distance to fault rupture	km
ė	Seismic erosion rate	mm yr ⁻¹
k_{sn}	Normalized channel steepness index	$m^{0.9}$
M_w	Earthquake moment magnitude	-
$N(M_w)$	Number of earthquakes in the magnitude bin $[M_w, M_w + 0.1]$	
R_0	Mean asperity depth	km
S_{mod}	Modal slope	0
t	Time period of multiple earthquake cycles	yr
T	Recurrence interval for Wenchuan-like earthquakes	yr
V_L	Landslide volume	m^3
$ heta_{ref}$	Reference concavity index	_
ω	Specific stream power	J m ⁻² yr ⁻¹

References

- 907 Ansberque, C., V. Godard, O. Bellier, J. De Sigoyer, J. Liu-Zeng, X. Xu, Z. Ren, Y. Li, and A. S. T. E.
- 908 R. Team (2015), Denudation pattern across the Longriba fault system and implications for the
- 909 geomorphological evolution of the eastern Tibetan margin, Geomorphology, 246, 542-557, doi:
- 910 10.1016/j.geomorph.2015.07.017.
- Arne, D., B. Worley, C. Wilson, S. F. Chen, D. Foster, Z. L. Luo, S. G. Liu, and P. Dirks (1997),
- Differential exhumation in response to episodic thrusting along the eastern margin of the Tibetan
- 913 Plateau, Tectonophysics, 280(3–4), 239-256, doi: 10.1016/S0040-1951(97)00040-1.
- 914 Bennett, G. L., S. R. Miller, J. J. Roering, and D. A. Schmidt (2016), Landslides, threshold slopes, and
- the survival of relict terrain in the wake of the Mendocino Triple Junction, Geology, doi:
- 916 10.1130/g37530.1.
- 917 Beaumont, C., R. A. Jamieson, M. H. Nguyen, and B. Lee (2001), Himalayan tectonics explained by
- 918 extrusion of a low-viscosity crustal channel coupled to focused surface denudation, Nature,
- 919 414(6865), 738-742, doi: 10.1038/414738a.
- Burchfiel, B. C., L. H. R., R.D. van der Hilst, B.H. Hager, Z. Chen, R.W. King, C. Li, J. Lü, H. Yao,
- and E. Kirby (2008), A geological and geophysical context for the Wenchuan earthquake of 12 May
- 922 2008, Sichuan, People's Republic of China, GSA Today, 18(7), 5, doi: 10.1130/GSATG18A.1.
- 923 Burbank, D. W., J. Leland, E. Fielding, R. S. Anderson, N. Brozovic, M. R. Reid, and C. Duncan
- 924 (1996), Bedrock incision, rock uplift and threshold hillslopes in the northwestern Himalayas, Nature,
- 925 379(6565), 505-510, doi:10.1038/379505a0.
- 926 Burbank, D. W., A. E. Blythe, J. Putkonen, B. Pratt-Sitaula, E. Gabet, M. Oskin, A. Barros, and T. P.
- Ojha (2003), Decoupling of erosion and precipitation in the Himalayas, Nature, 426(6967), 652-655,
- 928 doi:10.1038/nature02187.
- 929 Clark, M. K., and L. H. Royden (2000), Topographic ooze: Building the eastern margin of Tibet by
- lower crustal flow, Geology, 28(8), 703-706, doi:
- 931 10.1130/0091-7613(2000)28<703:tobtem>2.0.co;2.
- 932 CSN Catalog (2015), data collected by the China Seismograph Network stations, Copyrighted &
- produced by China Earthquake Networks Center (CENC)
- 934 (http://www.csndmc.ac.cn/wdc4seis@bj/earthquakes/csn_catalog_p001.jsp)
- Cui, J.W., J.G. Zhang, D. Gao, J.X. Duan and T. Wang (2012), The ground motion attenuation relation
- 936 for the Mountainous area in Sichuan and Yunnan, 15th World Conference on Earthquake
- 937 Engineering 2012, 1, 668-677.
- 938 Densmore, A. L., M. A. Ellis, Y. Li, R. J. Zhou, G. S. Hancock, and N. Richardson (2007), Active
- 939 tectonics of the Beichuan and Pengguan faults at the eastern margin of the Tibetan Plateau, Tectonics,
- 940 26(4), doi: 10.1029/2006tc001987.
- 941 Emberson, R., N. Hovius, A. Galy, and O. Marc (2016), Chemical weathering in active mountain belts
- controlled by stochastic bedrock landsliding, Nature Geoscience, 9(1), 42-45, doi:
- 943 10.1038/ngeo2600.
- 944 Gallen, S. F., M. K. Clark, and J. W. Godt (2015), Coseismic landslides reveal near-surface rock
- strength in a high-relief, tectonically active setting, Geology, 43(1), 11-14, doi: 10.1130/g36080.1.
- 946 Godard, V., J. Lave, J. Carcaillet, R. Cattin, D. Bourles, and J. Zhu (2010), Spatial distribution of
- denudation in Eastern Tibet and regressive erosion of plateau margins, Tectonophysics, 491(1-4),
- 948 253-274, doi: 10.1016/j.tecto.2009.10.026.

- Godard, V., R. Pik, J. Lave, R. Cattin, B. Tibari, J. de Sigoyer, M. Pubellier, and J. Zhu (2009), Late
- 950 Cenozoic evolution of the central Longmen Shan, eastern Tibet: Insight from (U-Th)/He
- 951 thermochronometry, Tectonics, 28, TC5009, doi: 10.1029/2008tc002407.
- Hovius, N., P. Meunier, L. Ching-Weei, C. Hongey, C. Yue-Gau, S. Dadson, H. Ming-Jame, and M.
- 953 Lines (2011), Prolonged seismically induced erosion and the mass balance of a large earthquake,
- 954 Earth and Planetary Science Letters, 304(3-4), 347-355, doi: 10.1016/j.epsl.2011.02.005.
- Hubbard, J., and J. H. Shaw (2009), Uplift of the Longmen Shan and Tibetan plateau, and the 2008
- 956 Wenchuan (M=7.9) earthquake, Nature, 458(7235), 194-197, doi: Doi 10.1038/Nature07837.
- Jarvis, A., H.I. Reuter, A. Nelson, E. Guevara, 2008, Hole-filled SRTM for the globe Version 4,
- available from the CGIAR-CSI SRTM 90m Database (http://srtm.csi.cgiar.org).
- 959 Jin, Z., A. J. West, F. Zhang, Z. An, R. G. Hilton, J. Yu, J. Wang, G. Li, L. Deng, and X. Wang (2016),
- 960 Seismically enhanced solute fluxes in the Yangtze River headwaters following the A.D. 2008
- 961 Wenchuan earthquake, Geology, 44(1), 47-50, doi: 10.1130/g37246.1.
- 962 Keefer, D. K. (1994), The Importance of Earthquake-Induced Landslides to Long-Term Slope Erosion
- and Slope-Failure Hazards in Seismically Active Regions, Geomorphology, 10(1-4), 265-284, doi:
- 964 10.1016/0169-555x(94)90021-3.
- 965 Kirby, E., P. W. Reiners, M. A. Krol, K. X. Whipple, K. V. Hodges, K. A. Farley, W. Tang, and Z. Chen
- 966 (2002), Late Cenozoic evolution of the eastern margin of the Tibetan Plateau: Inferences from
- 967 40Ar/39Ar and (U-Th)/He thermochronology, Tectonics, 21(1), doi: 10.1029/2000tc001246.
- Larsen, I. J., D. R. Montgomery, and O. Korup (2010), Landslide erosion controlled by hillslope
- 969 material, Nature Geoscience, 3(4), 247-251, doi: 10.1038/ngeo776.
- 270 Larsen, I. J., D. R. Montgomery, and H. M. Greenberg (2014), The contribution of mountains to global
- 971 denudation, Geology, doi: 10.1130/g35136.1.
- 2004), Denudation processes and rates in the Transverse Ranges, southern
- 973 California: Erosional response of a transitional landscape to external and anthropogenic forcing,
- 974 Journal of Geophysical Research: Earth Surface, 109(F1), 1-31, doi: 10.1029/2003jf000023.
- Li, G., A. J. West, A. L. Densmore, Z. Jin, R. N. Parker, and R. G. Hilton (2014), Seismic mountain
- 976 building: Landslides associated with the 2008 Wenchuan earthquake in the context of a generalized
- 977 model for earthquake volume balance, Geochemistry, Geophysics, Geosystems, 15(4), 833-844, doi:
- 978 10.1002/2013gc005067.
- 2016), Li, G., A. J. West, A. L. Densmore, D. E. Hammond, Z. Jin, F. Zhang, J. Wang, and R. G. Hilton (2016),
- 980 Connectivity of earthquake-triggered landslides with the fluvial network: Implications for landslide
- 981 sediment transport after the 2008 Wenchuan earthquake, Journal of Geophysical Research: Earth
- 982 Surface, 121(4), 703-724, doi: 10.1002/2015jf003718.
- 983 Liu, F, B.H. Fu, S.H. Yang (2013) Quantitative estimation of the evacuation time of landslide mass and
- 984 sediment induced by the 2008 Wenchuan great earthquake along the Minjiang River, Longmen Shan
- 985 in east Tibet, Chinese Journal of Geophysics, 56(5), 1517–1525. (in Chinese with English abstract)
- 986 Liu-Zeng, J., L. Wen, M. Oskin, and L. S. Zeng (2011), Focused modern denudation of the Longmen
- Shan margin, eastern Tibetan Plateau, Geochemistry Geophysics Geosystems, 12, Q1107, doi:
- 988 10.1029/2011gc003652.
- 989 Malamud, B. D., D. L. Turcotte, F. Guzzetti, and P. Reichenbach (2004), Landslides, earthquakes, and
- erosion, Earth and Planetary Science Letters, 229(1–2), 45-59, doi: 10.1016/j.epsl.2004.10.018.
- 991 Marc, O., N. Hovius, and P. Meunier (2016a), The mass balance of earthquakes and earthquake
- 992 sequences, Geophysical Research Letters, 43(8), 3708-3716, doi: 10.1002/2016gl068333.

- 993 Marc, O., N. Hovius, P. Meunier, T. Gorum, and T. Uchida (2016b), A seismologically consistent
- expression for the total area and volume of earthquake-triggered landsliding, Journal of Geophysical
- 995 Research: Earth Surface, 121(4), 2015JF003732, doi: 10.1002/2015jf003732.
- 996 Meunier, P., N. Hovius, and A. J. Haines (2007), Regional patterns of earthquake-triggered landslides
- and their relation to ground motion, Geophysical Research Letters, 34(20), L20408, doi
- 998 10.1029/2007gl031337.
- Molnar, P., and P. England (1990), Late Cenozoic uplift of mountain ranges and global climate change:
- 1000 chicken or egg?, Nature, 346(6279), 29-34, doi: 10.1038/346029a0.
- Molnar, P., W. R. Boos, and D. S. Battisti (2010), Orographic Controls on Climate and Paleoclimate of
- Asia: Thermal and Mechanical Roles for the Tibetan Plateau, Annual Review of Earth and Planetary
- 1003 Sciences, 38(1), 77-102, doi: 10.1146/annurev-earth-040809-152456.
- Montgomery, D. R., and M. T. Brandon (2002), Topographic controls on erosion rates in tectonically
- active mountain ranges, Earth and Planetary Science Letters, 201(3–4), 481-489, doi:
- 1006 10.1016/S0012-821X(02)00725-2.
- Ouimet, W. B. (2010), Landslides associated with the May 12, 2008 Wenchuan earthquake:
- 1008 Implications for the erosion and tectonic evolution of the Longmen Shan, Tectonophysics, 491(1-4),
- 1009 244-252, doi: 10.1016/j.tecto.2009.09.012.
- 1010 Ouimet, W. B., K. X. Whipple, and D. E. Granger (2009), Beyond threshold hillslopes: Channel
- adjustment to base-level fall in tectonically active mountain ranges, Geology, 37(7), 579-582, doi:
- 1012 10.1130/G30013a.1.
- 1013 Parker, R. N., A. L. Densmore, N. J. Rosser, M. de Michele, Y. Li, R. Q. Huang, S. Whadcoat, and D. N.
- Petley (2011), Mass wasting triggered by the 2008 Wenchuan earthquake is greater than orogenic
- growth, Nature Geoscience, 4(7), 449-452, doi: 10.1038/Ngeo1154.
- 1016 Raymo, M. E., W. F. Ruddiman, and P. N. Froelich (1988), Influence of late Cenozoic mountain
- building on ocean geochemical cycles, Geology, 16(7), 649-653, doi:
- 1018 10.1130/0091-7613(1988)016<0649:iolcmb>2.3.co;2.
- 1019 Reiners, P. W., and M. T. Brandon (2006), Using thermochronology to understand orogenic erosion,
- Annual Reviews of Earth and Planetary Scinces, 34, 419–466, doi:
- 1021 10.1146/annurev.earth.34.031405.125202.
- Richardson, N. J., A. L. Densmore, D. Seward, A. Fowler, M. Wipf, M. A. Ellis, L. Yong, and Y. Zhang
- 1023 (2008), Extraordinary denudation in the Sichuan Basin: Insights from low-temperature
- thermochronology adjacent to the eastern margin of the Tibetan Plateau, Journal of Geophysical
- 1025 Research: Solid Earth, 113(B4), doi: 10.1029/2006jb004739.
- 1026 Roback, K., M. Clark, A. J. West, D. Zekkos, G. Li, S. F. Gallen, D. Champlain, J. Godt (2017), The
- size, distribution, and mobility of landslides caused by the 2015 M_w7.8 Gorkha earthquake, Nepal,
- 1028 accepted, Geomorphology
- 1029 Shen, Z. K., J. B. Sun, P. Z. Zhang, Y. G. Wan, M. Wang, R. Burgmann, Y. H. Zeng, W. J. Gan, H. Liao,
- and Q. L. Wang (2009), Slip maxima at fault junctions and rupturing of barriers during the 2008
- Wenchuan earthquake, Nature Geoscience, 2(10), 718-724, doi: 10.1038/ngeo636.
- 1032 Steer, P., M. Simoes, R. Cattin, and J. B. H. Shyu (2014), Erosion influences the seismicity of active
- thrust faults, Nature Communications, 5, doi: 10.1038/ncomms6564.
- Thompson, T. B., A. Plesch, J. H. Shaw, and B. J. Meade (2015), Rapid slip-deficit rates at the eastern
- margin of the Tibetan Plateau prior to the 2008 Mw 7.9 Wenchuan earthquake, Geophysical
- 1036 Research Letters, 42(6), 1677-1684, doi: 10.1002/2014gl062833.

- 1037 Tian, Y., B. P. Kohn, A. J. W. Gleadow, and S. Hu (2013), Constructing the Longmen Shan eastern
- Tibetan Plateau margin: Insights from low-temperature thermochronology, Tectonics, 32(3), 576-592,
- 1039 doi: 10.1002/tect.20043.
- 1040 Utsu, T. (1999), Representation and Analysis of the Earthquake Size Distribution: A Historical Review
- and Some New Approaches, pure and applied geophysics, 155(2), 509-535, doi:
- 1042 10.1007/s000240050276.
- Vanmaercke, M., F. Ardizzone, M. Rossi, and F. Guzzetti (2017), Exploring the effects of seismicity on
- landslides and catchment sediment yield: An Italian case study, Geomorphology, 278, 171-183, doi:
- 1045 10.1016/j.geomorph.2016.11.010.
- 1046 Wang, E., E. Kirby, K. P. Furlong, M. van Soest, G. Xu, X. Shi, P. J. J. Kamp, and K. V. Hodges (2012),
- 1047 Two-phase growth of high topography in eastern Tibet during the Cenozoic, Nature Geoscience, 5(9),
- 1048 640-645, doi: 10.1038/ngeo1538.
- Wang, J., Z. Jin, R. G. Hilton, F. Zhang, A. L. Densmore, G. Li, and A. J. West (2015a), Controls on
- fluvial evacuation of sediment from earthquake-triggered landslides, Geology, 43(2), 115-118,doi:
- 1051 10.1130/g36157.1.
- Wang, J., Z. Jin, R. G. Hilton, F. Zhang, G. Li, A. L. Densmore, D. R. Gröcke, X. Xu, and A. J. West
- 1053 (2016), Earthquake-triggered increase in biospheric carbon export from a mountain belt, Geology,
- 1054 44(9), 44(9), doi: 10.1130/g37533.1.
- 1055 Wang, M., D. Jia, J. H. Shaw, J. Hubbard, A. Plesch, Y. Li, and B. Liu (2014), The 2013 Lushan
- earthquake: Implications for seismic hazards posed by the Range Front blind thrust in the Sichuan
- Basin, China, Geology, 42(10), 915-918, doi: 10.1130/g35809.1.
- Wang, Y., K. Zhang, Q. Gan, W. Zhou, L. Xiong, S. Zhang, and C. Liu (2015b), Bayesian probabilities
- of earthquake occurrences in Longmenshan fault system (China), Journal of Seismology, 19(1),
- 1060 69-82, doi: 10.1007/s10950-014-9451-2.
- 1061 West, A. J., R. Hetzel, G. Li, Z. Jin, F. Zhang, R. G. Hilton, and A. L. Densmore (2014), Dilution of
- 1062 ¹⁰Be in detrital quartz by earthquake-induced landslides: Implications for determining denudation
- rates and potential to provide insights into landslide sediment dynamics, Earth and Planetary Science
- 1064 Letters, 396(0), 143-153, doi: 10.1016/j.epsl.2014.03.058.
- 1065 Xu, C., X. Xu, X. Yao, and F. Dai (2014), Three (nearly) complete inventories of landslides triggered
- by the May 12, 2008 Wenchuan Mw 7.9 earthquake of China and their spatial distribution statistical
- analysis, Landslides, 11(3), 441-461, doi: 10.1007/s10346-013-0404-6.
- 1068 Xu, C., X. Xu, and J. B. H. Shyu (2015), Database and spatial distribution of landslides triggered by the
- Lushan, China Mw 6.6 earthquake of 20 April 2013, Geomorphology, 248, 77-92, doi:
- 1070 10.1016/j.geomorph.2015.07.002.
- Yang, S. L., K. H. Xu, J. D. Milliman, H. F. Yang, and C. S. Wu (2015), Decline of Yangtze River water
- and sediment discharge: Impact from natural and anthropogenic changes, Scientific reports, 5, 12581,
- 1073 doi: 10.1038/srep12581.

Supporting Information for

Earthquakes Drive Focused Denudation along a Tectonically Active Mountain Front

Gen Li^{1*}, A. Joshua West¹, Alexander L. Densmore², Zhangdong Jin³, Fei Zhang³, Jin Wang³, Marin Clark⁴, and Robert G. Hilton²

Email: genli@usc.edu; ligengeo@gmail.com

¹Department of Earth Sciences, University of Southern California, Los Angeles, CA 90089, USA

²Institute of Hazard, Risk and Resilience and Department of Geography, Durham University, Durham DH1 3LE, UK

³State Key Laboratory of Loess and Quaternary Geology, Institute of Earth Environment, Chinese Academy of Sciences, Xi'an 710075, China

⁴Department of Earth and Environmental Sciences, University of Michigan, Ann Arbor, MI 48109, USA

^{*}corresponding author

S1. Calculation of specific stream power

Specific stream power is calculated using the formula in Burbank et al. (2003):

$$\omega = \rho_{W} g Q G / W \tag{S1}$$

where ρ_w is the density of water, g is the gravitational acceleration, Q is water discharge (the product of upstream area and catchment area-normalized runoff), G is the channel gradient, and W is the channel width (calculated from an empirical scaling relation: $W = 10^{-2}Q^{0.4}$ [Burbank et a., 2003; Liu-Zeng et al., 2011; Ansberque et al., 2015]). Specific stream power is calculated for catchments with drainage area > 1 km², thought to be the regional threshold for fluvial channels [Li et al., 2016].

S2. Ratio between dissolved load and suspended load

Jin et al. (2016) reported the chemical composition of the dissolved load together with discharge at weekly frequency following the Wenchuan earthquake from two sites located on the Min Jiang river. Following Liu-Zeng et al. (2011), we calculate the daily dissolved load by multiplying the total concentrations of dissolved solids (mg L⁻¹ of Ca²⁺, Mg²⁺, K⁺, Na⁺, SiO₂, Cl⁻, SO₄²⁻, and HCO₃⁻) and the corresponding discharge (m³ day⁻¹). We interpolate the daily dissolved load and integrate the daily fluxes to get annual fluxes. The annual fluxes of the dissolved load are then compared to the fluxes of the suspended sediment. For the downstream Min Jiang site at Weizhou, the ratio between the total dissolved load and the suspended load is 30%, similar to the ratio reported before the Wenchuan earthquake (~35%, Chen et al., 2002). For the upstream Min Jiang site at Zhenjiangguan, the ratio is 75%, much higher than the downstream ratio. However, the drainage area upstream Zhenjiangguan only represents 6% of the total area of the studied catchments, whereas the drainage area upstream of Weizhou represents 28% of the total area (including areas above Zhenjiangguan), so we view the ratio at Weizhou as likely to be more representative. In a comprehensive compilation, Liu-Zeng et al. (2011) found a dissolved load:suspended load ratio of 35±15%, similar to our estimate for Weizhou. Combining these values, we calculate a mean ratio of 38±14% (Table S3).

The total dissolved load is corrected for atmospheric and anthropogenic inputs to obtain the denudation-derived dissolved load (i.e., from chemical weathering of rocks) using a coefficient of 49.5±2.5% (ratio of denudation-dissolved load to total dissolved load), as suggested by Liu-Zeng et al. (2011). This coefficient for the denudation-derived dissolved load has been estimated independently for the Min Jiang, Jialing Jiang (a neighboring river of the Min Jiang), Yangtze (Chang Jiang) and a compiled dataset of the global rivers, and the results from different studies are consistent around 50% [Summerfield and Hulton, 1994; Chetelat et al., 2008; Liu-Zeng et al., 2011 and references therein].

Finally, the ratio between the denudation-derived dissolved load and the suspended load is the product of the coefficient for the denudation component $(49.5\pm2.5\%)$ and the total dissolved load:suspended load ratio $(38\pm14\%)$, yielding a dissolved:suspended ratio for denudation of $19\pm7\%$ as reported in the main text.

S3. Threshold runoff for high magnitude runoff events

We examine the relationships between denudation rate and an index of high magnitude runoff events (the proportion of total runoff from events above a specified threshold runoff) across a wide range of runoff values (Figure S2). We find best correlations at a threshold runoff of 6 mm day⁻¹ for data from both before and after the Wenchuan earthquake.

S4. Principal component analysis (PCA) of studied metrics

The results of the PCA analysis are reported in Figure S5, Table S4, and Table S5. All metrics cluster into two groups: seismic (metrics with loading factor > 0.9) versus non-seismic (Table S4). These two groups explain > 85% of the total variance carried by the dataset (Table S5). The high magnitude runoff metric shows moderate correlation with both groups, but considering the physical meaning of this metric, we attribute it to the non-seismic group.

S5. Applying a global seismologically-based model to the Longmen Shan

Marc et al. (2016) derived a seismologically-based expression for the total volume of earthquake-triggered landslides, as:

$$V_L = \pi \overline{\delta}_V a_c R_0^2 A_{topo} \left(\frac{b\overline{S}}{R_0 a_c} - 1\right)^2 \left(\frac{L}{I_{asp}}\right) \exp\left(\frac{S_{mod}}{T_{SV}}\right), \quad (b\overline{S} > a_c R_0)$$
 (S2)

where V_L is the predicted landslide volume, $\bar{\delta}_V$ is an average material sensitivity term (global average = 4174±212 m³ km²), a_c is a critical acceleration to trigger landsliding (0.15±0.02 g), R_0 is the mean asperity depth (in the absence of data from rupture inversions, R_0 equals focal depth H for M_w <7.5 and half of focal depth H for Mw≥7.5), L is the fault rupture length (calculated using an empirical scaling relation reported below), I_{asp} is the characteristic length of an asperity (I_{asp} = 3km), S_{mod} is a modal slope angle determined from the slope histogram for specific cases, A_{topo} is the proportion of areas with sufficient steepness for landslide failure (slope angle > ~10°), T_{SV} is a steepness scaling constant (global average = 11.6±0.6°), b is the inferred source acceleration at a 1km distance from the source generating 1Hz seismic waves, and \overline{S} is an average amplification factor of seismic acceleration due to site effects. The term $b\overline{S}$ is calculated using equations Eq. S4 and Eq. S5, below [cf. Marc et al., 2016].

The fault rupture length is determined using an empirical scaling relation [Leonard, 2010]:

$$Log_{10}L = m_1 M_w + m_2 \tag{S3}$$

where m_1 and m_2 are scaling constants determined from the regression of a global dataset ($m_1 = 0.599, m_2 = -2.497$) [Leonard, 2010].

The term $b\overline{S}$ is determined as [cf. Marc et al., 2016]:

$$b\overline{S} = b_{sat}\overline{S} \exp(e_5(M_w - M_h) + e_6(M_w - M_h)^2), \quad (M_w \le M_h)$$
 (S4)

$$b\overline{S} = b_{sat}\overline{S} \exp(e_7(M_w - M_h)), \quad (M_w > M_h)$$
 (S5)

where M_h is a "hinge" magnitude (acceleration above this hinge magnitude saturates at b_{sat} , with $M_h = 6.75\pm0.1$), b_{sat} is the saturated value for acceleration at 1Hz, and e_5 , e_6 and e_7 are constants for 1Hz seismic waves (empirically determined from 58 worldwide earthquakes; $e_5 = 0.6728$, $e_6 = -0.1826$, $e_7 = 0.054$) [Boore and Atkinson, 2008; Marc et al., 2016]. $b_{sat}\bar{S}$ is chosen as 4000±400 m [Marc et al., 2016].

To apply this landslide volume model to specific cases, seismological parameters (L, R_0) and topographic parameters (S_{mod} , A_{topo}) need to be constrained independently, for example using local seismological and digital topographic data, respectively, whereas other parameters can be inferred from globally-averaged values [Marc et al., 2016], or if possible, calibrated for a specific region.

To apply the model to the Longmen Shan region, we use the Wenchuan and the Lushan cases (Wenchuan: focal depth $H=19\mathrm{km}$, $R_0=9.5\mathrm{km}$, $L=170\mathrm{km}$, $S_{mod}=31\pm4^\circ$, $A_{topo}=1$; Lushan: focal depth $H=R_0=14\mathrm{km}$, $L=20\mathrm{km}$, $S_{mod}=19\pm2.5^\circ$, $A_{topo}=0.8$) [Burchfiel et al., 2008; Zhang et al., 2014; Marc et al., 2016]. The uncertainties are calculated from 1,000,000 Monte Carlo random sampling simulations for each earthquake with specified magnitude. For each set of parameters, we calculate the results for 1000 earthquakes across a continuous range of magnitudes ($M_w=5-8$). The results are reported as the medians (the solid curves connecting 1000 data points on Figure 5b), and the 16^{th} and 84^{th} percentiles (the dashed curves on Figure 5b) of the Monte Carlo results.

Implementing this model across multiple earthquakes (i.e., to calculate a seismic erosion rate over simulated earthquake cycles) requires some estimate of the focal depth of each synthetic earthquake event. Using the Wenchuan and Lushan data, we fit a relation between M_w and focal depth of the form (following Leonard, 2010):

$$Log_{10}H = m_3M_w + m_4 \tag{S6}$$

where m_3 and m_4 are empirical scaling constants. This M_w -focal depth scaling relation is used for determining the focal depth and associated mean asperity depth when

applying the landslide volume model of Marc et al. (2016) over multiple synthetic earthquakes.

S6. Development of a seismologically-based model for the Longmen Shan

Using the Wenchuan ground motion and landslide dataset, we first establish the relationships between landslide volumetric density (volume of landslides in per unit area, m³ km⁻²) and peak ground accelerations (PGA). The landslide volumetric density is calculated every 2 km increment along the swath profile A-A'. PGA is calculated as the mean of the PGA data in the corresponding increment.

For the hanging wall (where >90% of the Wenchuan landslide volume is located), we find the relation best described using a power-law function ($r^2 = 0.82$) (Figure S3a):

$$Log_{10}\alpha_V = 7.24(PGA - 0.10)^{0.28}, (PGA > 0.1g)$$
 (S7)

where α_V is the landslide volumetric density.

For the footwall, we find the relationship is best described using a logarithmic function ($r^2 = 0.95$) (Figure S3a):

$$Log_{10}\alpha_V = 13.79PGA - 4.24,$$
 (PGA > 0.3g) (S8)

We then refer to a ground motion attenuation law to link PGA to earthquake magnitude and distance to the fault (Figure S3b) [Cui et al., 2012; Wang et al., 2015a]:

$$Log_{10}PGA = c_1 + c_2M_w + c_3Log_{10}(D + c_4)$$
(S9)

where D is the distance to the fault rupture, and c_1 , c_2 , c_3 and c_4 are empirical constants. Note that (1) this function is determined based on the ground motion data from seismic events in the Longmen Shan region and the neighboring areas [Cui et al., 2012; Wang et al., 2015a and references therein], and (2) we slightly modify the original law using the distance to fault rupture, replacing this term with the distance to hypocenter, assuming linear sources. This simplification still returns good fits for the Wenchuan ground motion data (Figure S3b). In applying Eq. S8, we thus use c_2 =0.21 as determined from regional regression [cf. Cui et al., 2012] and define c_1 , c_3 and c_4 using the Wenchuan ground motion data [USGS, 2008].

We next simulate ground motion for earthquakes occurring in the Longmen Shan region with specified magnitude using Eq. S8 and derive associated landslide volumes using Eq. S6 and Eq. S7. We calculate the volumes of landslides triggered by 20 earthquakes with different magnitudes from M_w =5 to M_w =8. We find the resulting

 M_w -landslide volume relation can be well described using a power-law function (Eq. 4 and Figure 5c in the main text).

S7. Estimating the probability of landslide-triggering for earthquakes

Some earthquakes may be too deep to trigger landslides. To evaluate how this effect influences seismic erosion rates calculated using the Longmen Shan specific model, we have excluded a proportion of earthquakes from the calculation. We determine probable earthquake depths with reference to the seismic catalog collected by the China Seismograph Network stations (1970-2015) [CSN catalog, 2015], which reports earthquake location, surface wave magnitude, local magnitude, and focal depth. We extract the earthquakes in the Longmen Shan region and convert all earthquake magnitudes to moment magnitudes (M_w) using the scaling relations reported in Wang et al. (2015a) and Scordilis (2006).

To assess the probability that an earthquake of a given magnitude would trigger landslides in this region, we use the Wenchuan and Lushan cases as defining the limiting conditions for landslide triggering. With reference to the earthquake magnitude-focal depth scaling relation calibrated by the Wenchuan and the Lushan data (Eq. S12), we assume the determined focal depth *H* is a characteristic depth for landslide-triggering. Earthquakes with focal depth deeper than this depth are assumed to generate little landslides, so the landslide-triggering probability of earthquakes is defined as the proportion of earthquakes with focal depth shallower than the corresponding characteristic depth (red curve in Figure S4a). Note that different thresholds for landslide triggering (i.e., different parameters in Eq. S12) would have limited affect on the conclusions of our study, since this correction for earthquake depth is small.

All the recorded earthquakes in the Longmen Shan region are then grouped by magnitude. The proportions of surface rupturing earthquakes are calculated for each magnitude bin containing > 40 events, which includes earthquakes with $M_w < \sim 5.6$, and we fit a non-linear relationship between M_w and the proportion of surface rupturing earthquakes (Figure S4b), assuming Wenchuan-like events have 100% probability of triggering landslides. We use this non-linear relationship as an estimate of the probability of earthquakes that can trigger landslides for a given magnitude and consequently adjust the seismic erosion rate. This approach provides an upper estimate for the magnitude of correction, since some earthquakes occurring at deeper depth may also trigger co-seismic landslides.

S8. Simulating earthquake sequences using a truncated Gutenburg-Richter relation

We use the *Caputo* equation [Utsu, 1999] as a truncated Gutenburg-Richter function to generate earthquake sequences:

$$\text{Log}_{10}n(M_w) = g_1 - g_2M_w - \text{Log}_{10}(1-10^{-g_2(g_3-M_w)}), \quad (M_w \le g_3 \text{ and } M_w \le M_{wmax}) \quad (S10)$$

$$n(M_w) = 0, \quad (M_w > M_{wmax} \text{ or } M_w > g_3)$$
 (S11)

where $n(M_w)$ is an exceedance frequency or the frequency (yr⁻¹) of earthquakes with magnitude $\geq M_w$, g_1 , g_2 and g_3 are empirical constants determined from regional seismicity data, and M_{wmax} is the maximum earthquake magnitude in the study area ($M_w = 7.9$ for the Longmen Shan).

The number of earthquakes with specified magnitudes over time t, $N(M_w)$, are calculated numerically as:

$$N(M_w) = t \times n(M_w) - t \times n(M_w + \Delta M_w)$$
 (S12)

where ΔM_w is set as 0.1 (cf. Keefer, 1994).

Supporting Information Figures and Tables

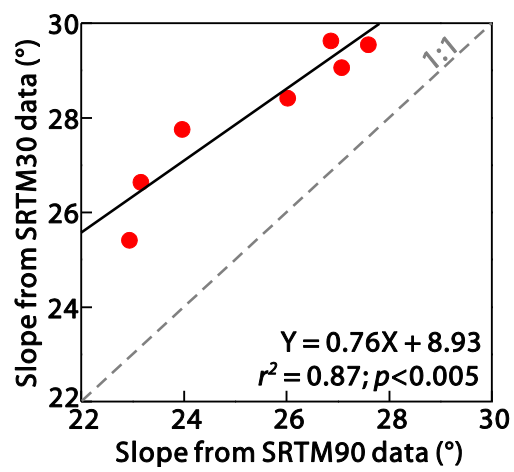


Figure S1. Correlations between slopes derived from SRTM30 DEM data versus SRTM90 DEM data for the seven studied catchments which have complete coverage of SRTM30 data. The red dots represent slope data. The black solid line denotes the best fit from the linear least square regression. The grey dashed line indicates 1:1 line.

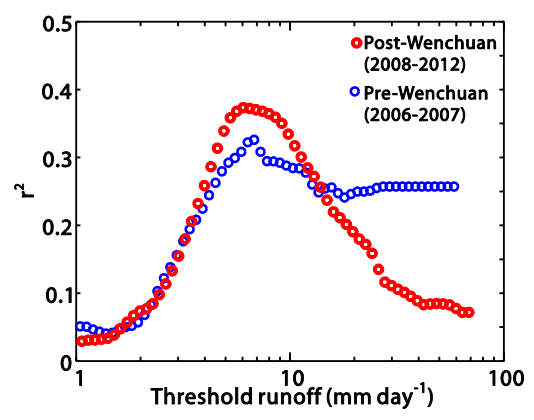


Figure S2. Threshold runoff versus the squares of correlation coefficient (r^2) between denudation rates and the proportion of total runoff from days > threshold value. The red dots indicate post-Wenchuan data (2008-2012). The blue dots indicate pre-Wenchuan data (2006-2007). Runoff data from Wang et al. (2015b).

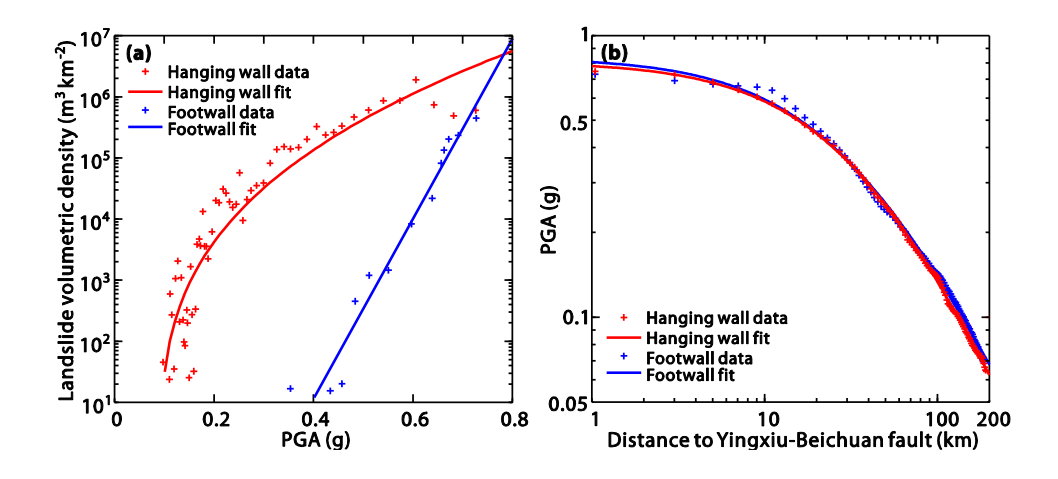


Figure S3. Relationships between landslide volumetric density and PGA for the Wenchuan earthquake, and between PGA and distance to fault. (a) Relationships between landslide volumetric density and PGA; (b) relationships between PGA and distance to the Yingxiu-Beichuan fault rupture. Red crosses and blue crosses are for the data from the hanging wall and from the footwall, respectively.

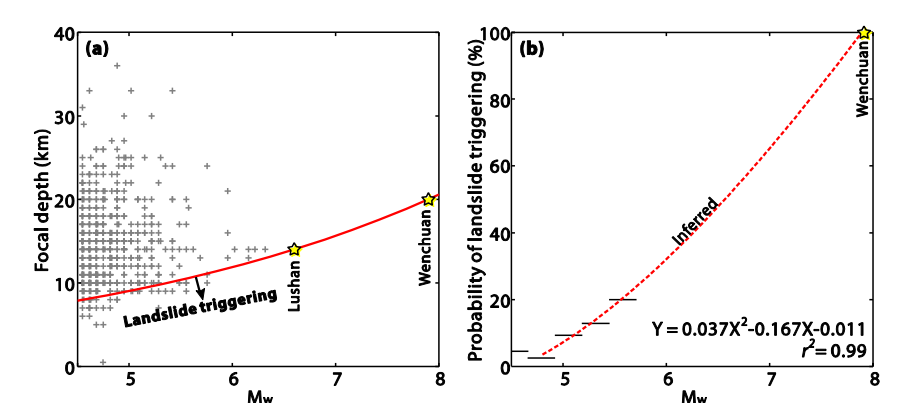


Figure S4. Earthquake magnitude, focal depth, and proportions of earthquakes rupturing to the surface in the study area. (a) Earthquake magnitude and corresponding focal depth for earthquakes from the China Seismograph Network catalog (1970-2015) in the study area; grey crosses refer to the seismic catalog data; the red curve represents a M_w -surface rupturing depth scaling relation calibrated by the Wenchuan and the Lushan earthquakes; (b) proportion of earthquakes that rupture the surface for magnitude-binned earthquakes in the seismic catalog; the black bars represent calculated proportions from (a); the red dashed lines represent inferred proportions from the least squares fit of the observed proportions $(M_w = 4.5-5.6)$ and from the assumption that earthquakes with magnitude of the Wenchuan event $(M_w = 7.9)$ would always trigger landslides.

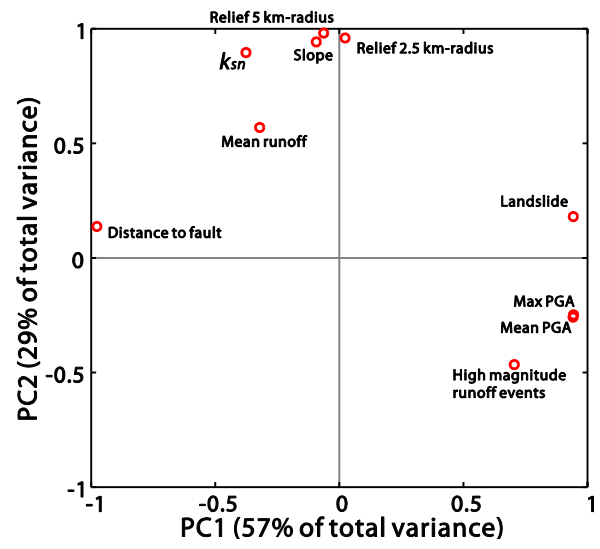


Figure S5. PCA plot for the studied metrics. Principle component (PC) 1 indicates the seismic component. PC2 corresponds to the non-seismic component.

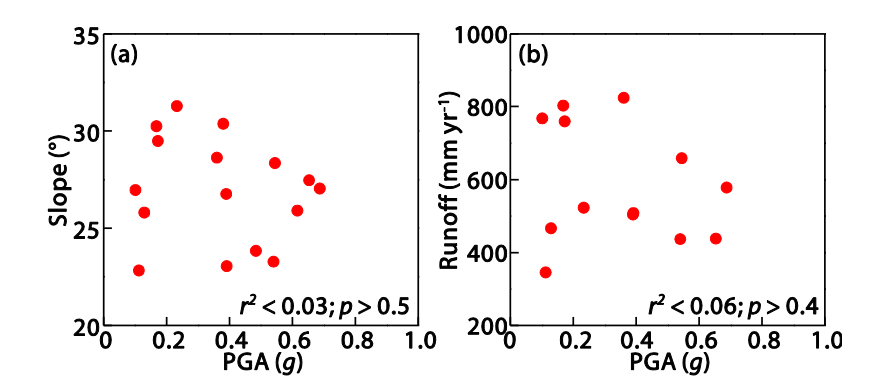


Figure S6. Relations between PGA, slope and runoff. (a) Catchment mean PGA vs. catchment mean slope; (b) Catchment mean PGA vs. catchment annual mean runoff. No statistically significant correlations are found between PGA and slope or runoff.

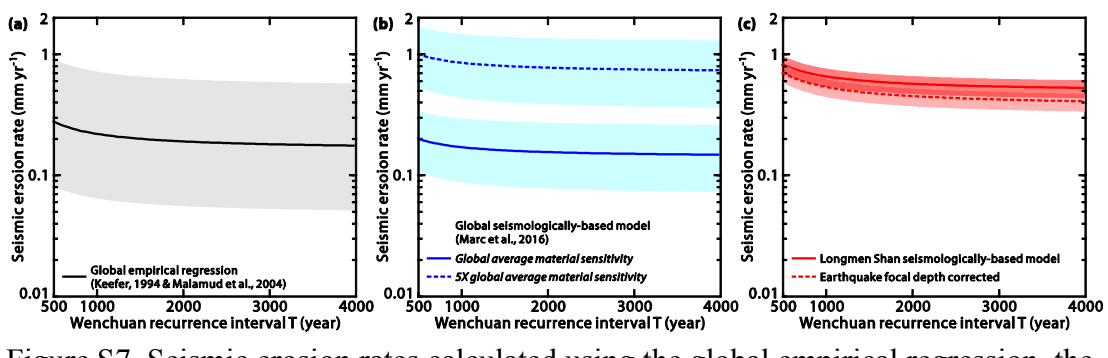


Figure S7. Seismic erosion rates calculated using the global empirical regression, the global seismologically-based model of Marc et al. (2016) with an adjusted material sensitivity term, and the Longmen Shan-specific model. (a) Seismic erosion rates calculated using the global empirical regression; the shaded area represent ±1 s.d. uncertainties; (b) seismic erosion rates calculated using the global seismologically-based model vs. T; the solid blue curve refers to the results using the global average material sensitivity; the dashed blue curve denotes the results with 5X increase in the material sensitivity; the shaded area represents 68% confidence interval from Monte Carlo simulations accounting for uncertainties of the relevant parameters, as reported in the Supplementary Information text (Marc et al., 2016); (c) seismic erosion rates calculated using the Longmen Shan landslide volume model vs. the recurrence interval of Wenchuan-like events (T), as also shown in Fig. 6b of the main text; the solid red curve denotes the results without focal depth-based correction for the probability of landslide-triggering; the dashed curve refers to the results with focal depth-based correction; the shaded area represent ±1 s.d. uncertainties.

Table S1. Denudation rates and metrics of topography, hydrology, fluvial transport capacity, and seismic processes associated with the Wenchuan earthquake of the studied catchments draining the Longmen Shan mountain range. (See separate excel file)

Table S2. Notation for symbols (including ones used in the Supporting Information)

Symbol	Notation	Unit
A	Area of landslide occurrence over earthquake cycles	km ²
a_c	Critical acceleration to trigger landslides	g
A_{topo}	Proportion of steep landscape	%
b	Inferred source acceleration at 1km	m
U	from the source with a given frequency (1 Hz)	m
b_{sat}	saturation acceleration for the scaling of b	m
$c_1 c_2 c_3 c_4$	Parameters of ground motion attenuation law, Longmen Shan	
D	Distance to fault rupture	km
ė	Seismic erosion rate	mm yr ⁻¹
$e_5 e_6 e_7$	Parameters of ground motion attenuation law, global	
G	Channel gradient	m m ⁻¹
g	Gravitational acceleration	
$g_1 g_2 g_3$	Parameters of truncated Guthenberg-Richter distribution	
H	Focal depth	km
I_{asp}	Characteristic length of asperity	km
k_{sn}	Normalized channel steepness index	$m^{0.9}$
L	Fault rupture length	km
$m_1 m_2$	Parameters of M_w -fault rupture length scaling relation	
$m_3 m_4$	Parameters of M_w -focal depth scaling relation	
M_h	Hinge magnitude	
M_w	Earthquake moment magnitude	
n(Mw)	Exceedance frequency of earthquakes with magnitude $> M_w$	yr ⁻¹
$N(M_w)$	Number of earthquakes in magnitude bin $[M_w, M_w + 0.1]$	
Q	Water discharge	m ³ year ⁻¹
R_{θ}	Mean asperity depth	km
\overline{S}	Average site effects on the amplification of acceleration	
S_{mod}	Modal slope	0
t	Time period of multiple earthquake cycles	Myr
T	Recurrence inteval for Wenchuan-like events	year
T_{SV}	Landscape steepness scaling constant	0
V_L	Landslide volume	m^3
W	Channel width	m
$\delta_{\scriptscriptstyle V}$	Material sensitivity to landsliding	$m^3 km^{-2}$
$ heta_{ref}$	Referene concavity index	
$ ho_w$	Density of water	
ω	Specific stream power	$J m^{-2} yr^{-1}$

Table S3. Compiled total dissolved load:suspended load ratios. Note only the two data from this study (Weizhou and Zhenjiangguan) are from after the 2008 Wenchuan earthquake. Other data are all from before the Wenchuan earthquake.

		Mean	Mean		
River	Station	annual	annual	Dissolved	
		suspended	dissolved	:	Reference
		load	load	suspended	
		(10^4 ton)	(10^4 ton)	ratio	
		year ⁻¹)	year ⁻¹)		
	Weizhou	807	245	0.30	Jin et al., 2016; this study (post-Wenchuan)
	Zhenjiangguan	64	48	0.75	Jin et al., 2016; this study (post-Wenchuan)
Min	Pengshan	1030	360	0.35	Liu-Zeng et al., 2011; Chen et al., 2002
Jiang	Duoyingping	935	210	0.22	Liu-Zeng et al., 2011; Chen et al., 2002
	Duoyingping	935	220	0.24	Liu-Zeng et al., 2011; Qin et al., 2006
	Jiajiang	1034	297	0.29	Liu-Zeng et al., 2011; Chen et al., 2002
	Shimian	1498	715	0.48	Liu-Zeng et al., 2011; Chen et al., 2002
	Yanrun	239	50	0.21	Liu-Zeng et al., 2011; Chen et al., 2002
	Wutongqiao	3470	1499	0.43	Liu-Zeng et al., 2011; Chen et al., 2002
	Qingshuixi	145	73	0.50	Liu-Zeng et al., 2011; Chen et al., 2002
	Gaochang	4950	1580	0.32	Liu-Zeng et al., 2011; Chen et al., 2002
	Xuankou	905	320	0.35	Liu-Zeng et al., 2011; Qin et al., 2006
	Sangping	172	67	0.39	Liu-Zeng et al., 2011; Qin et al., 2006
	Yibing	4950	1936	0.39	Liu-Zeng et al., 2011; Chetelat et al., 2008
	Gaocheng	4950	2202	0.44	Liu-Zeng et al., 2011; Qin et al., 2006
Dadu He	Luding	970	557	0.57	Liu-Zeng et al., 2011; Qin et al., 2006
Tuo Jiang	Sanhuangmiao	595	199	0.33	Liu-Zeng et al., 2011; Chen et al., 2002
Fu Jiang	Fujiangqiao	1086	195	0.18	Liu-Zeng et al., 2011; Chen et al., 2002
Yangtze	Datong	50000	17422	0.35	Liu-Zeng et al., 2011; Zhang et al., 1990
main	Wuhan	50000	22600	0.45	Liu-Zeng et al., 2011; Hu et al., 1982
			mean	0.38±0.14	

Table S4. Factor loading matrix from the PCA analysis (first two principle components or PCs explain > 85% of the total variance)

Metric	PC1	PC2	
Slope	-0.093	0.945	
Relief 5 km-radius	0.023	0.962	
Relief 2.5 km-radius	-0.063	0.984	
$\text{Log}_{10}k_{sn}$	-0.376	0.899	
Mean runoff	-0.321	0.572	
Proportion of total		-0.463	
runoff from high	0.705		
magnitude runoff events			
$(> 5 \text{ mm day}^{-1})$			
mean PGA	0.944	-0.246	
max PGA	0.942	-0.256	
distance to fault	-0.977	0.140	
Log ₁₀ landslide	0.943	0.183	
volumetric density			

Table S5. Total variance explained by the components

	% of	
Component	Variance	Cumulative %
1	57.598	57.598
2	29.330	86.929
3	7.166	94.095
4	2.925	97.020
5	1.607	98.628
6	0.848	99.475
7	0.280	99.755
8	0.212	99.967
9	0.025	99.992
10	0.008	100.000

References

- Ansberque, C., V. Godard, O. Bellier, J. De Sigoyer, J. Liu-Zeng, X. Xu, Z. Ren, Y. Li, and A. S. T. E. R. Team (2015), Denudation pattern across the Longriba fault system and implications for the geomorphological evolution of the eastern Tibetan margin, Geomorphology, 246, 542-557, doi: 10.1016/j.geomorph.2015.07.017.
- Boore, D. M., and G. M. Atkinson (2008), Ground-motion prediction equations for the average horizontal component of PGA, PGV, and 5%-damped PSA at spectral periods between 0.01 s and 10.0 s, Earthquake Spectra, 24(1), 99–138, doi:10.1193/1.28304
- Burchfiel, B. C., L. H. R., R.D. van der Hilst, B.H. Hager, Z. Chen, R.W. King, C. Li, J. Lü, H. Yao, and E. Kirby (2008), A geological and geophysical context for the Wenchuan earthquake of 12 May 2008, Sichuan, People's Republic of China, GSA Today, 18(7), 5, doi: 10.1130/GSATG18A.1.
- Chen, J. S., F. Y. Wang, X. H. Xia, and L. T. Zhang (2002), Major element chemistry of the Changjiang (Yangtze River), Chemical Geology, 187(3-4), 231-255, doi: 10.1016/S0009-2541(02)00032-3.
- Chetelat, B., C. Q. Liu, Z. Q. Zhao, Q. L. Wang, S. L. Li, J. Li, and B. L. Wang (2008), Geochemistry of the dissolved load of the Changjiang Basin rivers: Anthropogenic impacts and chemical weathering, Geochimica Cosmochimica Acta, 72(17), 4254-4277, doi: 10.1016/j.gca.2008.06.013.
- CSN Catalog (2015), data collected by the China Seismograph Network stations, Copyrighted & produced by China Earthquake Networks Center (CENC) (http://www.csndmc.ac.cn/wdc4seis@bj/earthquakes/csn_catalog_p001.jsp)
- Cui, J.W., J.G. Zhang, D. Gao, J.X. Duan and T. Wang (2012), The ground motion attenuation relation for the Mountainous area in Sichuan and Yunnan, 15th World Conference on Earthquake Engineering 2012, 1, 668-677.
- Jin, Z., A. J. West, F. Zhang, Z. An, R. G. Hilton, J. Yu, J. Wang, G. Li, L. Deng, and X. Wang (2016), Seismically enhanced solute fluxes in the Yangtze River headwaters following the A.D. 2008 Wenchuan earthquake, Geology, 44(1), 47-50, doi: 10.1130/g37246.1.
- Keefer, D. K. (1994), The Importance of Earthquake-Induced Landslides to Long-Term Slope Erosion and Slope-Failure Hazards in Seismically Active Regions, Geomorphology, 10(1-4), 265-284, doi: 10.1016/0169-555x(94)90021-3.
- Hu, M.-H., R. F. Stallard, and J. M. Edmond (1982), Major ion chemistry of some large Chinese rivers, Nature, 298(5874), 550-553, doi:10.1038/298550a0.
- Leonard, M. (2010), Earthquake fault scaling: Self-consistent relating of rupture length, width, average displacement, and moment release, Bulletin of the Seismological Society of America, 100(5A), 1971-1988, doi: 10.1785/0120090189.
- Li, G., A. J. West, A. L. Densmore, D. E. Hammond, Z. Jin, F. Zhang, J. Wang, and R. G. Hilton (2016), Connectivity of earthquake-triggered landslides with the fluvial network: Implications for landslide sediment transport after the 2008 Wenchuan earthquake, Journal of Geophysical Research: Earth Surface, 121(4), 703-724, doi: 10.1002/2015jf003718.
- Liu-Zeng, J., L. Wen, M. Oskin, and L. S. Zeng (2011), Focused modern denudation of the Longmen Shan margin, eastern Tibetan Plateau, Geochemistry Geophysics Geosystems, 12, Q1107, doi: 10.1029/2011gc003652.

- Marc, O., N. Hovius, P. Meunier, T. Gorum, and T. Uchida (2016), A seismologically consistent expression for the total area and volume of earthquake-triggered landsliding, Journal of Geophysical Research: Earth Surface, 121(4), 2015JF003732, doi: 10.1002/2015jf003732.
- Scordilis, E. M. (2006), Empirical Global Relations Converting M S and m b to Moment Magnitude, Journal of Seismology, 10(2), 225-236, doi: 10.1007/s10950-006-9012-4.
- Summerfield, M. A., and N. J. Hulton (1994), Natural controls of fluvial denudation rates in major world drainage basins, Journal of Geophysical Research: Solid Earth, 99(B7), 13871-13883, doi: 10.1029/94jb00715.
- USGS Earthquake Hazard Program, 2008 May 12 06:28:01 UTC. (http://earthquake.usgs.gov/earthquakes)
- Utsu, T. (1999), Representation and Analysis of the Earthquake Size Distribution: A Historical Review and Some New Approaches, Pure and Applied Geophysics, 155(2), 509-535, doi: 10.1007/s000240050276.
- Wang, Y., K. Zhang, Q. Gan, W. Zhou, L. Xiong, S. Zhang, and C. Liu (2015a), Bayesian probabilities of earthquake occurrences in Longmenshan fault system (China), Journal of Seismology, 19(1), 69-82, doi: 10.1007/s10950-014-9451-2.
- Wang, J., Z. Jin, R. G. Hilton, F. Zhang, A. L. Densmore, G. Li, and A. J. West (2015b), Controls on fluvial evacuation of sediment from earthquake-triggered landslides, Geology, 43(2), 115-118, doi: 10.1130/g36157.1.
- Zhang, Y., R. Wang, Y.-T. Chen, L. Xu, F. Du, M. Jin, H. Tu, and T. Dahm (2014), Kinematic rupture model and hypocenter relocation of the 2013 Mw 6.6 Lushan earthquake constrained by strong-motion and teleseismic data, Seismological Research Letters, 85(1), 15–22, doi:10.1785/0220130126.
- Zhang, J., W. W. Huang, M. G. Liu, and Q. Zhou (1990), Drainage basin weathering and major element transport of two large Chinese rivers (Huanghe and Changjiang), Journal of Geophysical Research: Oceans, 95(C8), 13277-13288, doi: 10.1029/JC095iC08p13277.